Zhao *et al. Energy Mater* 2025;5:500004
DOI: 10.20517/energymater.2024.48

Energy Materials

Review

Open Access

Check for updates

MXenes and their composites for advanced cathodes in multivalent ion batteries

Xiaoru Zhao[1,#], Chunpeng Ruan[1,#], Yuanhua Sang[1], Shuhua Wang[1,*], Hong Liu[1,2,*]

[1]State Key Laboratory of Crystal Materials, Shandong University, Jinan 250100, Shandong, China.
[2]Jinan Institute of Quantum Technology, Jinan Branch, Hefei National Laboratory, Jinan, 250101, Shandong, China.
[#]Authors contributed equally.

***Correspondence to:** Dr. Shuhua Wang, State Key Laboratory of Crystal Materials, Shandong University, Shanda South Road 27, Jinan 250100, Shandong, China. E-mail: wangshuhua2019@sdu.edu.cn; Dr. Hong Liu, State Key Laboratory of Crystal Materials, Shandong University, Shanda South Road 27, Jinan 250100, Shandong, China. E-mail: hongliu@sdu.edu.cn

How to cite this article: Zhao X, Ruan C, Sang Y, Wang S, Liu H. MXenes and their composites for advanced cathodes in multivalent ion batteries. *Energy Mater* 2025;5:500004. https://dx.doi.org/10.20517/energymater.2024.48

Received: 19 May 2024 **First Decision:** 21 Jun 2024 **Revised:** 12 Jul 2024 **Accepted:** 17 Jul 2024 **Published:** 30 Jul 2024

Academic Editor: Yun Zhang **Copy Editor:** Fangling Lan **Production Editor:** Fangling Lan

Abstract

In recent years, multivalent metal-ion batteries (MMIBs) have garnered significant attention and research interest because of their abundant natural reserves, low cost, and high safety. However, in practical applications, owing to the high charge density of multivalent metal ions and the strong interaction between the intercalated metal ion and the cathode, the cathode exhibits low capacity and poor cycle stability. Therefore, it is crucial to explore suitable cathode materials for use in MMIBs. MXenes are novel two-dimensional materials that have developed rapidly in the field of energy storage. The current use of MXenes as cathodes in MMIBs has not yet been systematically summarized. This review summarizes the evolution and achievements of MXene-based cathodes in MMIBs, including MXenes and their derivatives, MXene/transition metal oxide composites, MXene/sulfur-based material composites, MXene/selenium-based material composites, and other MXene composites. Finally, the current challenges and future development of MXenes for advanced cathodes in MMIBs are discussed.

Keywords: MXenes, MXene composite materials, cathodes, multivalent metal-ion batteries

INTRODUCTION

Large-scale development and utilization of fossil fuels have caused resource shortages and environmental pollution[1,2]. Traditional energy-storage technologies cannot meet the needs of social development[3].

Therefore, there is a global consensus on reducing dependence on traditional energy sources and developing clean and renewable energy resources[4]. Efficient storage of clean energy is crucial to ensure a reliable and sustainable energy supply[5]. Lithium-ion batteries (LIBs) are recognized as the most prevalent energy-storage devices owing to their exceptional energy density and cycling stability[6,7]. However, limited lithium resources, high costs, and unsafe and toxic organic electrolytes have triggered the search for more secure and stable energy-storage devices[8].

In recent years, multivalent metal-ion batteries (MMIBs) have undergone rapid development[9]. An outstanding feature of multivalent metals, such as zinc (Zn), aluminum (Al), magnesium (Mg), and calcium (Ca), is their ability to transfer multiple electrons during reactions[10]. Moreover, multivalent metals have many advantages, including abundant natural reserves, low cost, and high safety, making them a favorable choice for large-scale energy storage[11]. Therefore, researchers have shifted their focus to the investigation of MMIBs. However, several challenges remain associated with the use of MMIBs. Although the diameters of multivalent metal ions are similar to those of lithium ions, the high charge density of multivalent metal ions can generate strong Coulombic interactions with the crystal lattice of the cathode material, leading to high energy barriers that may induce adverse changes, such as irreversible phase transition, dissolution of active materials, and structural collapse of the cathode material[12,13]. Therefore, enhancing the conductivity of the cathode materials and expanding the space that can accommodate ions are crucial for optimizing the electrochemical performance of MMIBs.

MXenes, which are typical layered two-dimensional (2D) materials, have the advantages of outstanding electrical conductivity[14], high specific surface area[15], superior mechanical properties[16,17], excellent chemical stability[18], and strong adjustability[19]. To date, the applications of MXenes in advanced batteries have been extensively summarized and discussed. The utilization of MXenes and their derivatives in aqueous batteries has been comprehensively reviewed, including cathodes, anodes, and electrolytes[20-23]. In addition, the applications of MXenes in anodes have been carefully summarized, focusing on modification strategies employed by MXenes for stable and dendrite-free metal anodes[24,25]. With the rise of MMIBs, a review of the applications of MXenes in MMIBs involving the cathode and anode has been published[26]. However, to the best of our knowledge, a comprehensive review of MXenes as advanced cathodes for MMIBs has not yet been conducted. MXenes are primarily utilized as cathode materials in Zn-ion batteries (ZIBs), Al-ion batteries (AIBs), and Mg-ion batteries (MIBs). For Ca-ion batteries (CIBs), Ca^{2+} has a high coordination number (8), whereas MXenes exhibit a low-coordination environment[13]. Therefore, storing Ca^{2+} in MXenes is difficult. To date, no studies on MXenes in CIBs have been reported. It is an opportune moment to summarize the research progress and analyze the future directions of the application of MXenes as cathodes in MMIBs.

In this review, we summarize the evolution and accomplishments of MXenes as advanced cathodes for MMIBs. First, we provide an overview of the advantages and synthesis methods for MXenes. Subsequently, we discuss and summarize the applications of MXenes as cathodes in MMIBs, including MXenes and their derivatives, MXene/transition metal oxide composites, MXene/sulfur-based material composites, MXene/selenium-based material composites, and other MXene composites [Figure 1]. Finally, we offer insights into the development prospects of MXenes as cathodes for MMIBs.

MXENES

MXenes are typical layered 2D materials containing transition metal carbides, nitrides, and carbonitrides[27]. The general chemical formula is $M_{n+1}X_nT_x$ (n = 1-4), where M denotes the early transition metal, such as titanium (Ti), vanadium (V), molybdenum (Mo), chromium (Cr), and zirconium (Zr), X represents carbon,

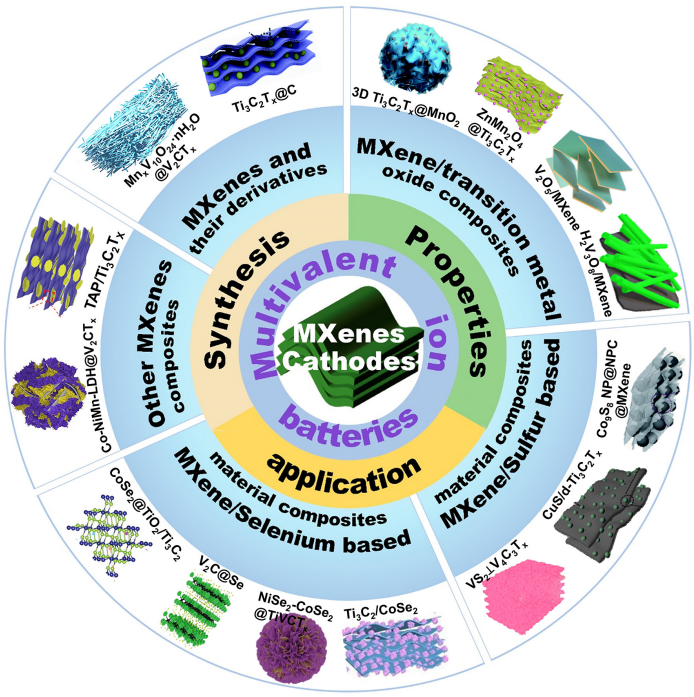

Figure 1. Schematic for the application of MXenes and their composites as advanced cathodes in MMIBs.

nitrogen, or carbonitrides, and T_x denotes the surface functional group of the MXenes [Figure 2]. The functional group is typically represented by -OH, -O, -F, and -Cl[28,29]. MXenes and their derivatives have garnered considerable attention from researchers because of their unique structures, particularly in the field of electrochemical energy storage. Notably, the M elements in MXenes that are currently used as cathodes in MMIBs are Ti, V, and Nb. Therefore, it is necessary to explore other MXenes as cathodes for their potential application.

Advantages of MXenes

Physical properties of MXenes

An outstanding advantage of MXenes and their derivatives is their high electrical conductivity, which plays a vital role in enhancing ion and electron transfer. The $Ti_3C_2T_x$ film was reported to exhibit an impressive electrical conductivity value of approximately 9,880 S cm^{-1} with a thin film thickness of 88 nm[14]. In addition, the 2D structure of MXenes has a high specific surface area and aspect ratio. This unique structure allows for better contact between the electrolyte and the electrode material, creating more active sites for electrochemical reactions. The nitrogen-doping $Ti_3C_2T_x$ has been reported to have an open pore structure and a high specific surface area of up to 368.8 $m^2 g^{-1}$[15], while its MAX phase is only 5.1 $m^2 g^{-1}$.

Additionally, MXenes exhibit excellent strength and toughness. They can withstand high external loads and stresses without breaking or deforming. MXenes also exhibit remarkable hardness, which allows them to withstand scratches and abrasions caused by external forces. A 5-mm-thick hollow $Ti_3C_2T_x$ cylinder can withstand 4,000 times its own weight[16]. Flexible $Ti_3C_2T_x$ MXene paper has been reported to have a tensile strength of 83.2 MPa and a conductivity of 265,600 S m^{-1} and can be folded into small windmills[30]. These characteristics make MXenes an excellent electrode choice for flexible batteries and wearable electronics.

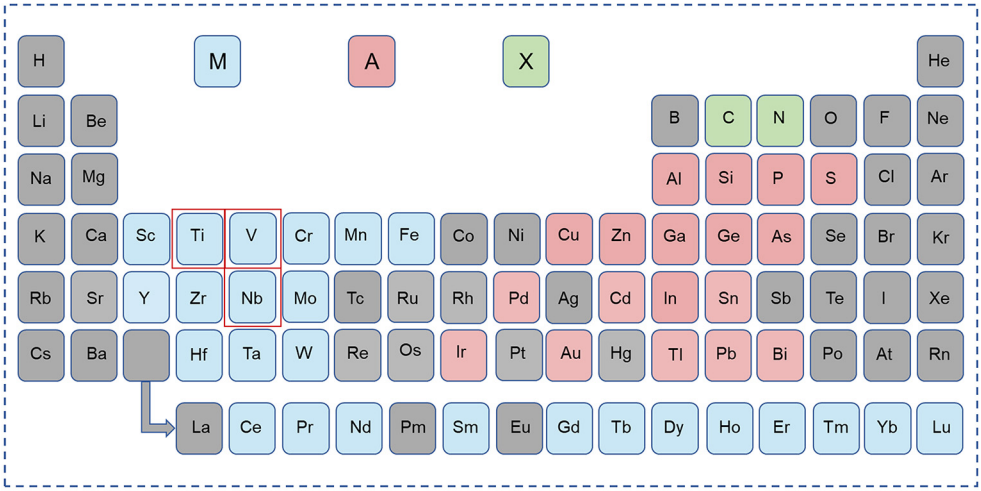

Figure 2. Periodic table fragments illustrating "M", "A", and "X" elements of the MAX phases.

Chemical properties of MXenes

The remarkable chemical stability of MXenes makes them ideal for energy-storage devices, maintaining stability even in complex electrolyte environments[18]. This extends the lifespan of the devices and enhances their reliability and durability. Additionally, their negatively charged surface can be easily combined with other positively charged materials through an electrostatic self-assembly strategy[27], and the layered structure of MXenes enables electrodes to expose more active sites for charge storage, further enhancing their potential for energy-storage applications[31]. A heterostructure material (Cu-HHTP/MX) composed of Cu-HHTP (HHTP = 2,3,6,7,10,11-hexahydroxytriphenylene) and V_2CT_x MXene was prepared via electrostatic self-assembly[31]. Brunauer-Emmett-Teller (BET) results show that Cu-HHTP/MX has a larger surface area (152.6 $m^2 g^{-1}$) than Cu-HHTP (90.88 $m^2 g^{-1}$), suggesting that MXene can increase the number of active sites for the insertion/extraction of Zn^{2+} ions.

MXene materials can be tailored to meet specific performance requirements by adjusting their elemental compositions and terminal functional groups (T_x), such as -O, -OH, and -F. According to the reports[32,33], owing to fluorine-containing acid etching, the surface terminations of MXenes inevitably generate abundant -F, which hinders Zn^{2+} ion transfer in ZIBs. To solve this problem, OH-termination-rich V_2CT_x material was prepared through a one-step alkalization method[34]. The tailored MXene realized fast Zn^{2+} ion transfer, exhibiting outstanding electrochemical performance (498.2 mA h g^{-1} at 0.1 A g^{-1}, and 195.1 mA h g^{-1} at 30 A g^{-1}) and excellent cycle stability (96.2% capacity retention upon 20,000 cycles).

Synthesis methods for MXenes

"Top-down" selective etching method

The "top-down" method removes the A-layer atoms in the MAX phase through direct or indirect chemical etching and then peels them to form single- or multilayer MXene nanosheets. Most MXenes are currently obtained using the "top-down" method, and the typical synthesis method is hydrofluoric acid (HF) etching. $Ti_3C_2T_x$ was first synthesized using a HF solution to etch the Al layer of the Ti_3AlC_2 MAX phase, as shown in Figure 3A[35]. During the synthesis of MXenes, some crucial parameters exist, such as the HF concentration, etching time, and reaction temperature[36]. However, the strong corrosiveness and toxicity of HF render the preparation process dangerous. Other fluorine-based etchers have also been investigated. A mixture of hydrochloric acid (HCl) and lithium fluoride (LiF) as an alternative to HF was reported to synthesize $Ti_3C_2T_x$ successfully [Figure 3B][37]. The resulting MXene is a clay-like product that can be used to prepare

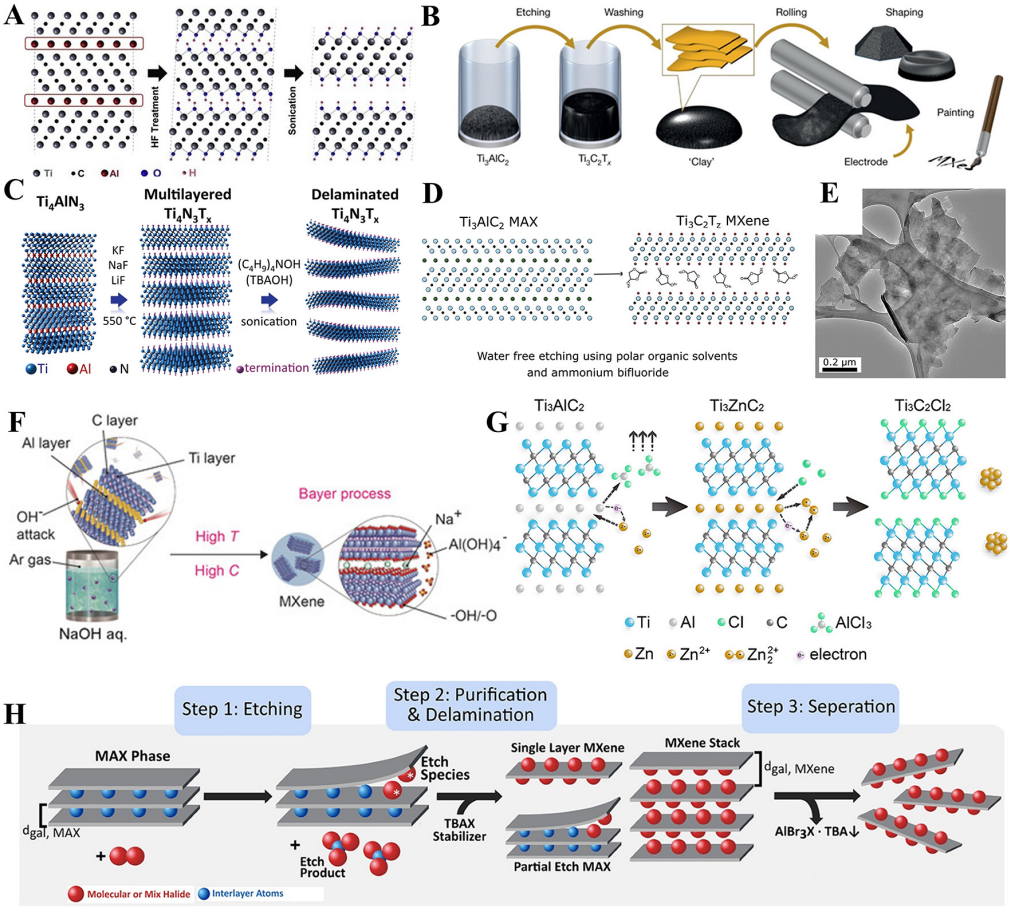

Figure 3. (A) Schematic illustration of the synthesis of $Ti_3C_2T_x$ by HF. This figure is quoted with permission from Naguib *et al.* Copyright (2011) John Wiley and Sons[35]. (B) Schematic illustration of the preparation of $Ti_3C_2T_x$ by HCl + LiF. This figure is quoted with permission from Ghidiu *et al.* Copyright (2014) Springer Nature[37]. (C) Schematic illustration of the preparation of $Ti_4N_3T_x$ by high-temperature molten salt method. This figure is quoted with permission from Urbankowski *et al.* Copyright (2016) RSC Pub[42]. (D) Schematic illustration of the synthesis of $Ti_3C_2T_x$ by organic polar solvents. (E) TEM image of delaminated $Ti_3C_2T_x$ sheets etched by organic polar solvents. This figure is quoted with permission from Natu *et al.* Copyright (2020) Elsevier[43]. (F) Schematic illustration of the preparation of $Ti_3C_2T_x$ by alkali etching. This figure is quoted with permission from Li *et al.* Copyright (2018) John Wiley and Sons[45]. (G) Schematic illustration of the synthesis of $Ti_3C_2T_x$ by Lewis acidic molten melts etching. This figure is quoted with permission from Li *et al.* Copyright (2019) American Chemical Society[46]. (H) Schematic illustration of the preparation of $Ti_3C_2T_x$ by halogen etching. This figure is quoted with permission from Jawaid *et al.* Copyright (2021) American Chemical Society[47].

various electrodes and films. Since then, other fluorinated salts (NaF[38,39], KF[39], NH_4F[39,40], and FeF_3[41]) have proven useful for the synthesis of MXenes. In addition to aqueous solution etching, MXenes have also been synthesized using the high-temperature molten salt method. The specific approach is to heat the salt mixture (29 wt% LiF, 59 wt% KF, and 12 wt% NaF) and Ti_4AlN_3 at 550 °C for 30 min under an argon (Ar) atmosphere to produce $Ti_4N_3T_x$ [Figure 3C][42]. Organic solvents have also been used for water-free etching of MXenes. According to the literature[43], NH_4HF_2 can be dissociated into HF and NH_4F in polar organic solvents (such as propylene carbonate [PC], N-methyl-2-pyrrolidone [NMP], and dioxane [DXN]). Therefore, Ti_3AlC_2 was etched using organic polar solvents in the presence of NH_4HF_2 to obtain $Ti_3C_2T_z$ MXene, which expanded the use of MXene in water-sensitive applications [Figure 3D]. The transmission electron microscope (TEM) image in Figure 3E shows a typical $Ti_3C_2T_z$ flake morphology, indicating the successful preparation of MXene.

Although the application of fluorine-based etchers (such as HCl + LiF, salt mixture (LiF + KF + NaF), and NH_4HF_2) reduces operational risk, it inevitably leads to environmental pollution. Consequently, researchers have redirected their focused on the synthesis of fluorine-free MXenes. Electrochemical etching has been demonstrated as an effective approach. $Ti_3C_2T_x$ was obtained by anodic corrosion[44]. The Al atoms on the anode side of the MAX phase were extracted and subsequently replaced with hydroxide groups in the NH_4Cl and TMAOH electrolytes. Notably, electrochemical etching utilizes a two-electrode system and no etching reactions occur at the cathode. Alkali etching has also been found to be useful for the synthesis of MXenes. It has been reported that $Ti_3C_2T_x$ MXene can be obtained using NaOH (27.5 M) at 270 °C to etch Ti_3AlC_2, and the purity of $Ti_3C_2T_x$ is as high as 92% [Figure 3F][45]. Furthermore, the utilization of Lewis acid to remove Zn atoms from the MAX phase is an effective method for synthesizing MXenes. It requires the transformation from the MAX phase to a Zn-based MAX phase at 550 °C in an Ar atmosphere via the replacement reaction [Figure 3G][46]. The resulting Ti_3ZnC_2 reacts with $ZnCl_2$ to form a chlorine (Cl)-terminated MXene. Considering the high-temperature conditions of Lewis acid, milder halogen etching has been proposed. For example, Ti_3AlC_2 was etched using halogens (Br_2, I_2, ICl, and IBr) in anhydrous media [Figure 3H][47].However, this type of etching can be affected by various factors such as the absolute concentration of the halogen, temperature, the solvent, and the molar ratio of the halogen to the MAX phase.

"Bottom-up" direct synthesis method

In the "bottom-up" method, MXenes are directly synthesized without etching the MAX phase. Synthesized MXenes have the advantages of a large size and few defects[48]. Chemical vapor deposition (CVD) was the first direct synthesis method for MXenes. Mo_2C MXene was synthesized by reacting Mo atoms from Mo foil with carbon atoms produced from methane at a temperature above 1,085 °C[49]. Mo_2C is a chemically stable crystal with a size exceeding 100 μm and a thickness of several nanometers. In addition to conventional CVD systems, large-area Mo_2C MXene has been grown using plasma-enhanced pulsed laser deposition[50]. This method combines the advantages of both plasma-enhanced CVD and pulsed laser deposition. The temperature required for this crystal growth is 700 °C, and the laser pulse number can control crystal thickness. In addition, MXenes can be directly synthesized using the salt-templated method. MoO_3-coated NaCl was first synthesized using an Mo precursor and NaCl under an Ar atmosphere at 280 °C, and then MoO_3-coated NaCl was ammoniated under an NH_3 atmosphere at 650 °C to generate MoN MXene[51]. However, large-scale application of MXenes is hindered by the low output, high equipment requirements, and high cost of the "bottom-up" method[48]. Therefore, it is important to explore more efficient methods for expanding the applications of MXenes.

APPLICATION OF MXENES FOR CATHODE MATERIALS IN MMIBS

MXenes and their derivatives as cathodes

MXenes have developed rapidly in the field of energy storage. They have outstanding electrical conductivity[14], high specific surface area[15], superior mechanical properties[16,17], excellent chemical stability[18], and strong adjustability[19]. However, owing to the strong hydrogen bonds and interlayer van der Waals forces of MXenes, they tend to agglomerate and stack during cycling, leading to a reduction in active sites and acceleration of structural collapse [Figure 4][52]. Moreover, owing to the strong interactions between multivalent ions and MXenes, metal ions exhibit a high diffusion energy barrier during intercalation/deintercalation from MXenes. For example, pure Ti_3C_2 MXenes cannot store Mg ions and exhibit zero capacity in MIBs[53]. Therefore, to reduce the aggregation of MXenes and the migration barrier of ions, it is necessary to modify pure MXenes to improve their electrochemical performance.

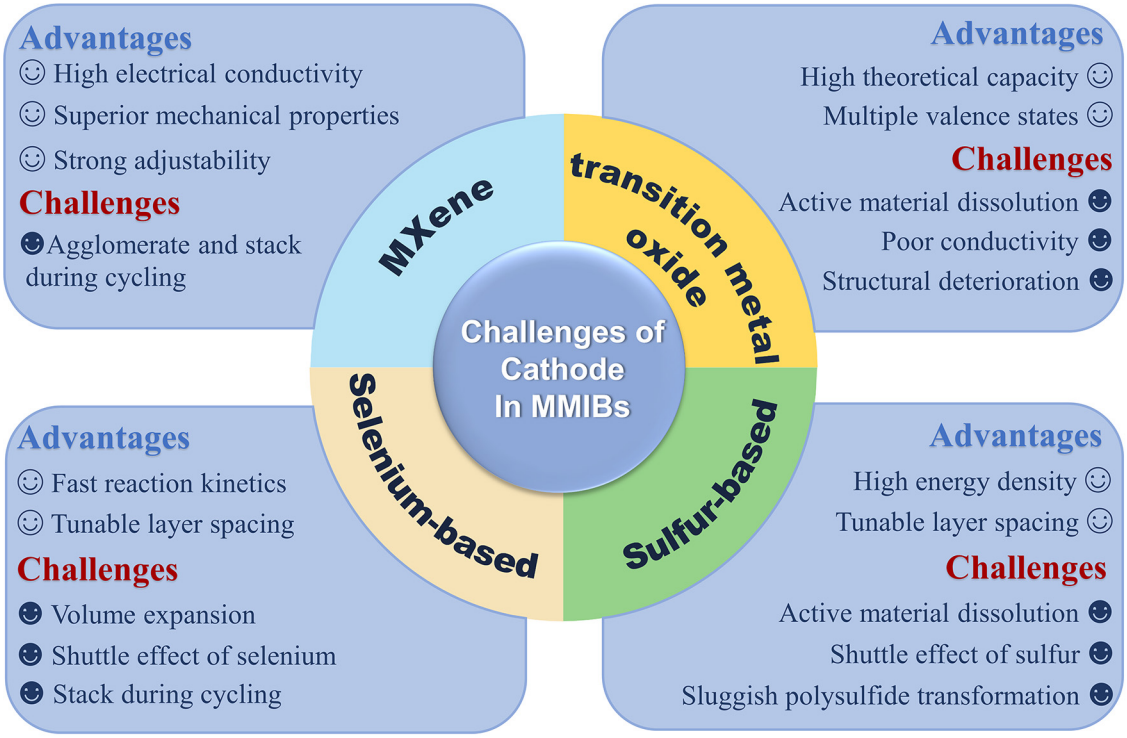

Figure 4. Schematic illustration of advantages and challenges of cathodes in MMIBs.

MXenes and their derivatives as cathodes in ZIBs

ZIBs have attracted considerable interest because of their eco-friendliness, cost-effectiveness, and safety[54-57]. The Zn anode has a high theoretical specific capacity (820 mA h g^{-1} and 5,851 mA h cm^{-3}), a low redox potential [-0.763 V *vs.* Standard Hydrogen Electrode (SHE)], and abundant reserves, making it an ideal large-scale energy-storage device[58,59]. In the past few years, 2D MXenes have been extensively researched in ZIBs because of their high metal conductivity (close to graphene: 10^5-10^6 S m^{-1}), large layer spacing, structural stability, controllable surface functional groups, *etc.*

Although MXenes have many properties required for ZIB cathodes, the large amount of F surface terminations produced in the traditional fluoric acid etching process usually leads to high hydrophobicity and slow ion diffusion kinetics, which deteriorates the electrochemical performance. Therefore, the replacement of -F functional groups with functional groups that are hydrophilic (-OH) or electrochemically active (-I, -Br) is expected to improve the performance of MXenes. A novel OH-rich terminal V_2CT_x material with interlayer "K^+-pillars" (alk-V_2CT_x) was proposed [Figure 5A][34]. According to the X-ray diffraction (XRD) patterns [Figure 5B], the (002) peak of alk-V_2CT_x shifted to a smaller angle, indicating that the inserted K^+ ions increased the layer spacing[60]. Simultaneously, the inserted K^+ ions improved the structural stability of the alk-V_2CT_x cathode. Owing to the large number of hydrophilic -OH terminations, the hydrophilicity of alk-V_2CT_x was significantly better than that of traditional HF-etched V_2CT_x [Figure 5C], which is conducive to electrolyte infiltration in the electrode. The alk-V_2CT_x cathode had a specific capacity of 498.2 mA h g^{-1} at 0.1 A g^{-1}, with a capacity retention of 96.2% after 20,000 cycles at 10 A g^{-1}.

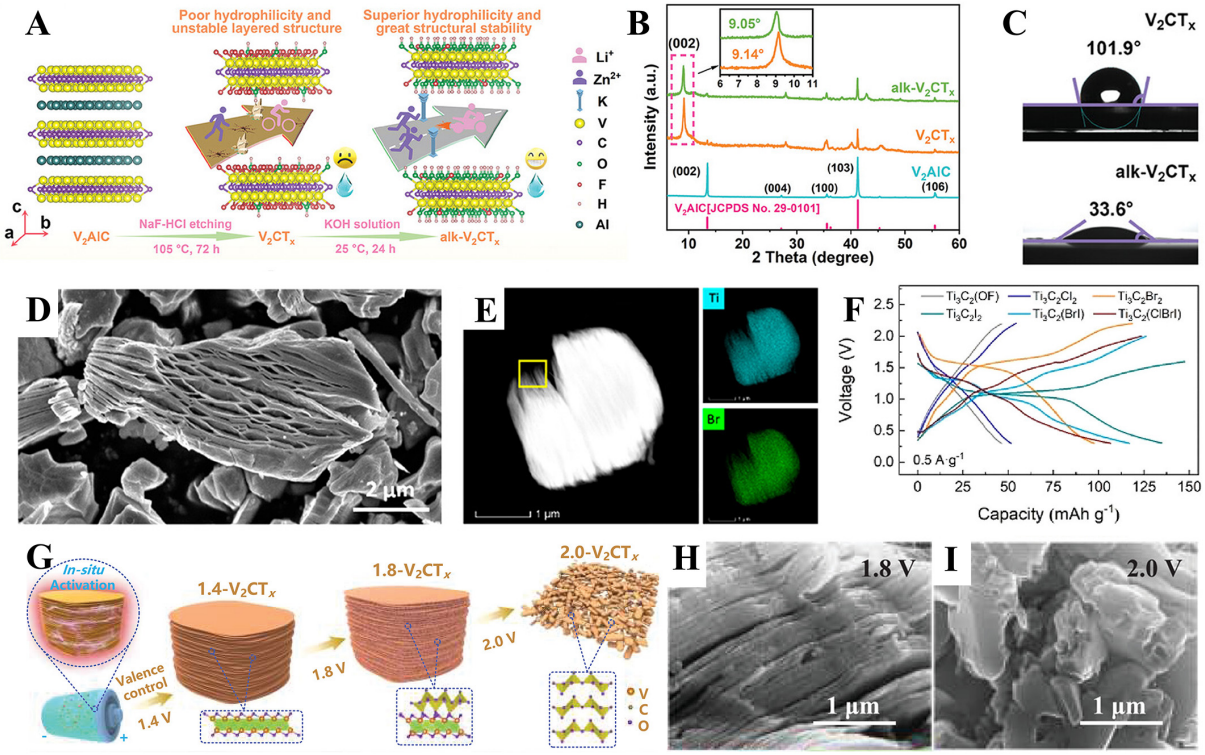

Figure 5. (A) Illustration of hydrophilicity and structural stability's improvement of alk-V_2CT_x. (B) XRD patterns of V_2AlC, V_2CT_x, and alk-V_2CT_x. (C) Comparison of hydrophilicity between V_2CT_x and alk-V_2CT_x. This figure is quoted with permission from Chen *et al.* Copyright (2023) John Wiley and Sons[34]. (D) SEM image of $Ti_3C_2Br_2$. (E) HAADF-STEM image and EDS mappings of $Ti_3C_2Br_2$. (F) Charge and discharge curves of halogenated Ti_3C_2 MXenes at 0.5 A g^{-1}. This figure is quoted with permission from Li *et al.* Copyright (2021) American Chemical Society[61]. (G) Schematic illustration of V_2CT_x cathodes at different voltages by *in-situ* electrochemical activation. (H and I) SEM images of V_2CT_x cathodes after electrochemical activation at 1.8 V and 2.0 V. This figure is quoted with permission from Liu *et al.* Copyright (2020) John Wiley and Sons[62].

In addition to -OH terminations, various halogen terminals (such as -Cl and -Br) can improve the electrochemical properties of MXene. Ti_3C_2 MXenes with different halogen terminals were obtained by etching with different copper halide molten salts at high temperatures[61]. After etching the Al layers, the scanning electron microscopy (SEM) image of $Ti_3C_2Br_2$ [Figure 5D] exhibited a multilayer structure similar to that of $Ti_3C_2(OF)$ MXene (obtained via traditional HF etching), indicating successful halogenated MXene etching. The high-angle annular dark-field scanning transmission electron microscopy (HAADF-STEM) image and energy-dispersive spectroscopy (EDS) elemental mapping [Figure 5E] showed that bromine (Br) was uniformly distributed on $Ti_3C_2Br_2$. According to the galvanostatic charge and discharge (GCD) curves of Ti_3C_2 MXenes with different halogen terminals [Figure 5F], $Ti_3C_2Br_2$ had a specific capacity of 97.6 mA h g^{-1} and a discharge platform of 1.6 V, whereas $Ti_3C_2I_2$ had a specific capacity of 135 mA h g^{-1} and a discharge platform of 1.1 V. However, $Ti_3C_2Cl_2$ and $Ti_3C_2(OF)$ both exhibited low capacity (51.7 and 46.5 mA h g^{-1}, respectively). The electron transfer between Br^- (I^-) and Br^0 (I^0) provides voltage platforms and higher capacity than $Ti_3C_2Cl_2$ and $Ti_3C_2(OF)$, indicating that the surface chemical adjustment of MXenes is important for improving their electrochemical performance.

Compared with other MXenes, V_2C MXenes uniquely benefit from the multiple valence states of V and the high specific capacity of V-based cathodes. The oxidation of low-valence V in V_2C to obtain MXene-based derivatives is a unique method for enhancing the electrochemical properties of V_2C MXenes. The low-valence V in the V_2CT_x cathode was oxidized from V^{2+}/V^{3+} to V^{4+}/V^{5+} through initial charging activation,

forming a nanoscale V oxide (VO_x) coating and achieving more Zn-ion storage[62]. Currently, electrochemical activation, hydrothermal oxidation, and selenization are used to prepare MXene-based derivatives. V_2CT_x MXene cathodes have been held at different voltages for 2 h, and the obtained products were denoted as 1.4-V_2CT_x, 1.8-V_2CT_x, and 2.0-V_2CT_x [Figure 5G]. Among these MXenes, the outer surface of 1.8-V_2CT_x was coated with homogeneous nanoscale VO_x and the internal V-C-V multilayer structure was retained, whereas 2.0-V_2CT_x was over-oxidized [Figure 5H and I]. Activated high-valence V species provide additional capacity, and internally retained V-C-V layers ensure high conductivity of the cathodes. Thus, the 1.8-V_2CT_x cathode had a specific capacity of 358 mA h g^{-1} even at 30 A g^{-1}. In contrast to traditional acid and alkali etching, an *in-situ* electrochemical method that removes the Al layer and enhances the V valence of V_2AlC has been proposed[63]. During the electrochemical process, the V_2AlC cathode undergoes three sequential stages [Figure 6A]. (1) The Al layer is exfoliated by the fluorine-rich electrolyte; (2) V is gradually oxidized to V_2O_5; and (3) After a long cycle, the V_2O_5 particles are uniformly distributed on the retained carbon layer, leading to the formation of a V_2O_5/C/V_2O_5 structure. The resulting V_2O_5/C/V_2O_5 sandwich structure is shown in Figure 6B. The XRD patterns [Figure 6C] of the V_2AlC cathode after long-term cycling also demonstrate the presence of V_2O_5 particles and carbon layers. The obtained cathode had a capacity of 409.7 mA h g^{-1} at 0.5 A g^{-1} and 95.7 mA h g^{-1} at 64 A g^{-1}.

The electrochemical properties of cathodes can also be effectively enhanced through ion insertion. MXene-derived materials intercalated with metal ions (such as Mg^{2+}[64] and Zn^{2+}[65]) have also been extensively studied. Based on the significant ion-adsorption capacity of MXenes, V_2CT_x was alkalized with KOH (K-V_2CT_x). The $Mn_xV_{10}O_{24}{\cdot}nH_2O$@$V_2CT_x$ heterostructure (MVO@VC) was then synthesized from K-V_2CT_x by hydrothermal Mn^{2+} intercalation and oxidation [Figure 6D][66]. Through the hydrothermal process, K-V_2CT_x transformed from its original layered structure to a three-dimensional (3D) porous network structure [Figure 6E and F]. The MVO@VC cathode has a capacity of 287.6 mA h g^{-1} at 10 A g^{-1} and a retained 92.9% initial capacity after 25,000 cycles. Generally, the induction of V_2C MXene using electrochemical methods to obtain MXene-based derived materials is time-consuming and uncontrollable; thus, a simple surface selenization strategy has been proposed[67]. As shown in Figure 6G, transition metal selenides were obtained from the surface layer of MXenes using selenium powder as an oxidant in an Ar atmosphere, whereas the inner layers of MXene remained. In this study, VSe_2@V_2CT_x nanohybrid was successfully synthesized. In addition to V_2CT_x, the successful selenization of $Ti_3C_2T_x$ ($TiSe_2$@$Ti_3C_2T_x$) and Nb_2CT_x ($NbSe_2$@Nb_2CT_x) suggests that this approach is suitable for a broad range of MXenes. On the one hand, the presence of V_2CT_x facilitates ion and electron diffusion; on the other hand, VSe_2, with a stable structure, increases the capacity. The VSe_2@V_2CT_x cathode had a capacity of 231.3 mA h g^{-1} after 100 cycles at 0.5 A g^{-1} and 158.1 mA h g^{-1} after 600 cycles at 2.0 A g^{-1}.

MXenes and their derivatives as cathodes in AIBs

Al metal reserves are abundant. Al is the world's most productive non-ferrous metal and can be processed easily. In addition, Al metal anodes exhibit a high theoretical capacity of 2,980 mA h g^{-1}. Consequently, rechargeable AIBs have emerged as a promising energy-storage technology owing to their cost-effectiveness, superior safety, and high energy density[68,69]. However, a shortage of suitable cathode materials hinders the development of AIBs. The use of 2D MXenes as cathode materials in AIBs has been extensively studied. Metal ions such as Li^+[70], Na^+[71], K^+[72], Mg^{2+}[53], and Al^{3+}[73] can be inserted into MXene layers, providing new opportunities for MMIBs that lack high-capacity and stable cathode materials[74].

V_2CT_x MXene was used as a cathode, and its reaction mechanism in AIBs is shown in Figure 7A. During discharging process, the $[Al_2Cl_7]^-$ ions dissociate into $[AlCl_4]^-$ and Al^{3+} ions at the cathode/electrolyte interface, followed by the insertion of Al^{3+} ions into the MXene layers. For the anode, the Al metal

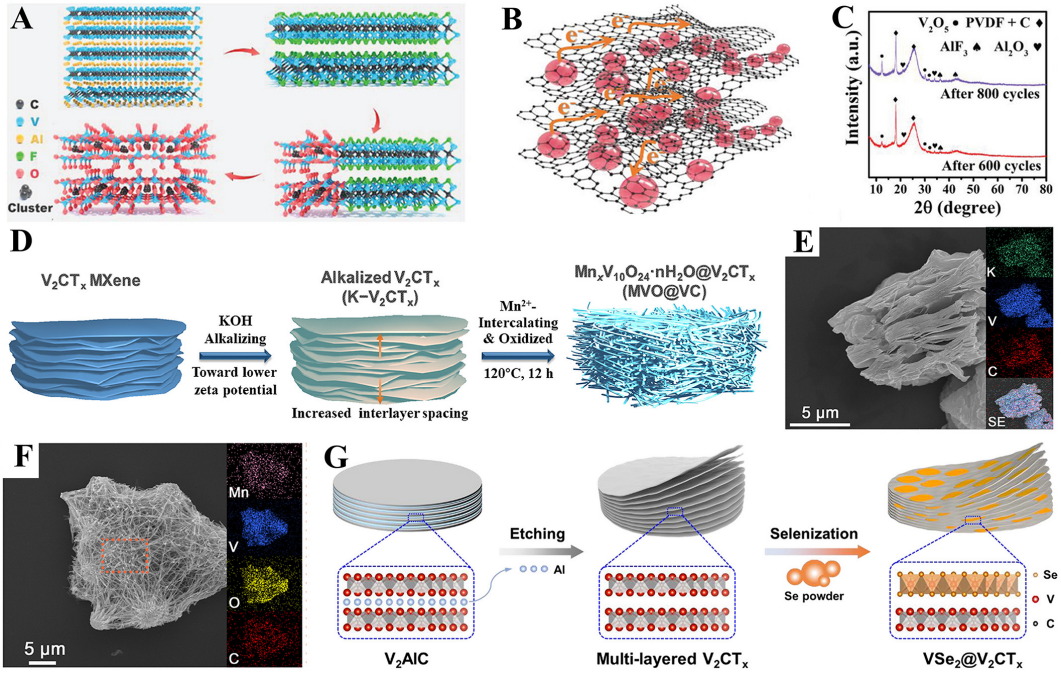

Figure 6. (A) Schematic diagram of electrochemical activation of V_2AlC cathode at 5 A g^{-1}. (B) Schematic diagram of the resulting uniform distribution of V_2O_5 particles on two-dimensional carbon layers. (C) XRD patterns of V_2AlC cathode after long cycling at 5 A g^{-1}. This figure is quoted with permission from Li *et al.* Copyright (2020) John Wiley and Sons[63]. (D) Schematic illustration of ion intercalation and oxidation process during MVO@VC preparation. (E) SEM image of K-V_2CT_x with the element mapping. (F) SEM image of MVO@VC with the element mapping. This figure is quoted with permission from Zhu *et al.* Copyright (2021) Elsevier[66]. (G) Schematic representation of the synthetic process for $VSe_2@V_2CT_x$ nanohybrids. This figure is quoted with permission from Sha *et al.* Copyright (2022) American Chemical Society[67].

undergoes a chemical reaction with $[AlCl_4]^-$ ions, resulting in the formation of $[Al_2Cl_7]^-$ ions. Although the etching process removes the Al layers in MXenes, most MXene layers remain in the state of multilayer stacking, which is unfavorable for ion transport and reaction kinetics. The use of interpolators to further delaminate MXenes and increase the layer spacing can improve the ion-storage capacity. Fewer-layer V_2CT_x (TBAOH-FL-V_2CT_x) [Figure 7B] was the formation of multiple-layer V_2CT_x (ML-V_2CT_x) [Figure 7C] after treatment with tetrabutylammonium hydroxide (TBAOH)[75]. The XRD pattern [Figure 7D] shows that the interlayer spacing of TBAOH-FL-V_2CT_x increased by 5.73 Å compared to ML-V_2CT_x without TBAOH treatment. More uniform delamination endows the TBAOH-FL-V_2CT_x cathode with better electrochemical performance. The TBAOH-FL-V_2CT_x cathode had a discharge capacity of 300 mA h g^{-1} at 0.1 A g^{-1}. In contrast, that of the ML-V_2CT_x cathode was approximately 100 mA h g^{-1} under the same conditions.

Based on single-layer MXene obtained by TBAOH treatment [Figure 7E], Li *et al.* adjusted the single-layer Nb_2CT_x MXene surface terminated species and removed interlayer water molecules by calcination, enhancing the capacity and cycle life of the cathode[73]. The large layer spacing (1.22 nm) caused by etching and delamination is conducive to ion transport in AIBs. In addition, the XRD patterns [Figure 7F] show that Nb_2CT_x MXene generated Nb_2O_5 and amorphous carbon after calcination, which likely contributed to the improved capacity and cycling performance of the cathode[76,77]. After calcination at 200 °C, the C-Nb_2CT_x (200 °C-calcined Nb_2CT_x MXene) cathode had a capacity of 108 mA h g^{-1} at 0.2 A g^{-1} and maintained ~85% initial capacity after 500 cycles. However, under the same conditions, the specific discharge capacity of the P-Nb_2CT_x (pristine single-layered Nb_2CT_x MXene) cathode decreased to ~76 mA h g^{-1} after 300 cycles.

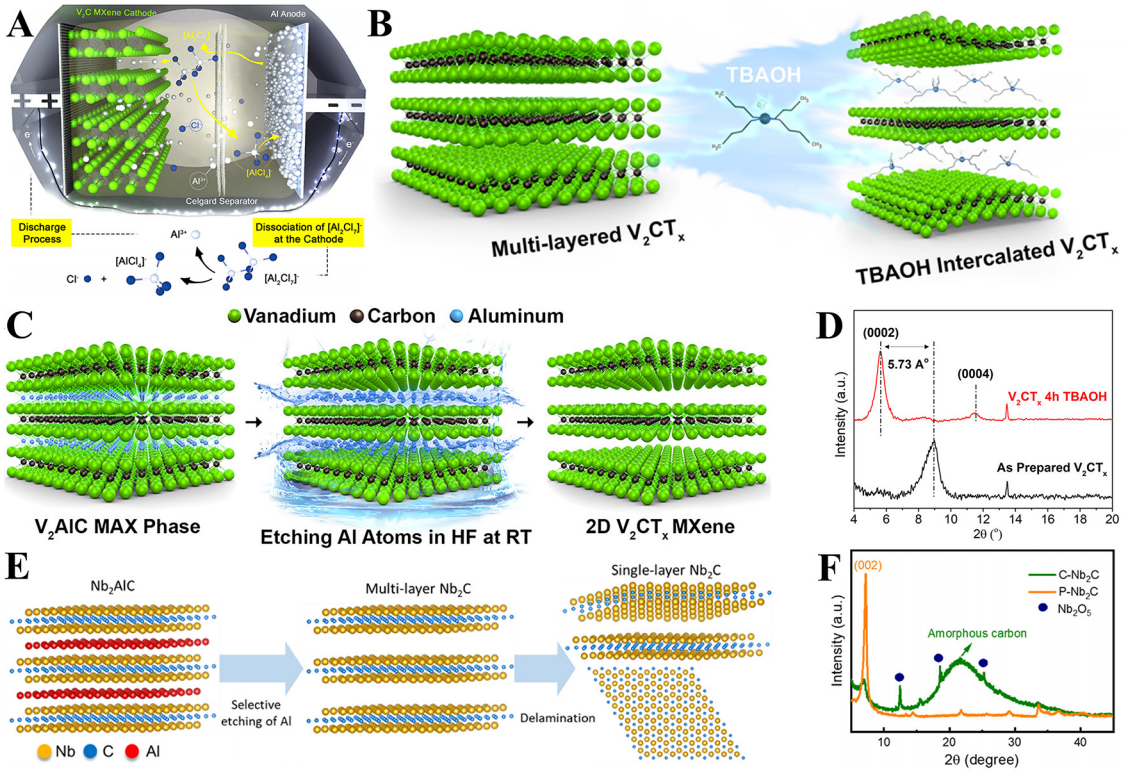

Figure 7. (A) Schematic representation of the reaction mechanism of the AIBs with V_2CT_x MXene as the cathode. (B) Schematic representation of TBAOH intercalation to increase ML-V_2CT_x MXene layer spacing. (C) Schematic representation of ML-V_2CT_x etching process. (D) XRD patterns of ML-V_2CT_x and TBAOH-FL-V_2CT_x. This figure is quoted with permission from VahidMohammadi *et al.* Copyright (2017) American Chemical Society[75]. (E) Schematic representation of preparing single-layer Nb_2CT_x MXene. (F) XRD patterns of P-Nb_2CT_x and C-Nb_2CT_x. This figure is quoted with permission from Li *et al.* Copyright (2022) American Chemical Society[73].

MXenes and their derivatives as cathodes in MIBs

As an emerging advanced energy-storage technology, MIBs have garnered significant research interest, mainly because Mg is abundant (approximately 10^4 times that of lithium), has a lower redox potential (-2.36 V *vs.* SHE), and has an ultra-high volumetric capacity of up to 3,833 mA h cm^{-3} (*vs.* 2,046 mA h cm^{-3} for a lithium anode)[78]. In addition, Mg is insensitive to moisture and air, making it more convenient for manufacturing MIBs. Mg metal, as an anode, also exhibits less dendrite growth during electrochemical deposition because of the strong bonding of Mg atoms and fast ion mobility[79]. However, the diffusion kinetics of Mg^{2+} are considerably slower because of the strong interactions between Mg^{2+} ions and cathode materials[10]. Consequently, MIBs exhibit low capacity and poor cycle life. Current research is focused on identifying suitable cathode materials to improve the performance of MIBs.

MXene materials have a unique layered structure that can be used directly as cathodes for Mg-ion storage in MIBs. To promote the reversible removal of Mg ions from MXenes, cetyltrimethylammonium bromide (CTAB) pre-intercalated Ti_3C_2 MXene was proposed as a cathode[53]. Density functional theory (DFT) verified that CTA^+ can facilitate charge transfer to MXenes, thereby enhancing the migration kinetics of Mg atoms on the MXene surface, leading to a significant change in capacity from a value close to zero to a considerable value (300 mA h cm^{-3} at 50 mA g^{-1}, Figure 8A). In addition to CTAB, carbon nanospheres have been proven to be effective intercalated materials for enhancing the performance of MXenes. Sandwich-structured MXene@C nanospheres were prepared via electrostatic interactions between $Ti_3C_2T_x$ and carbon

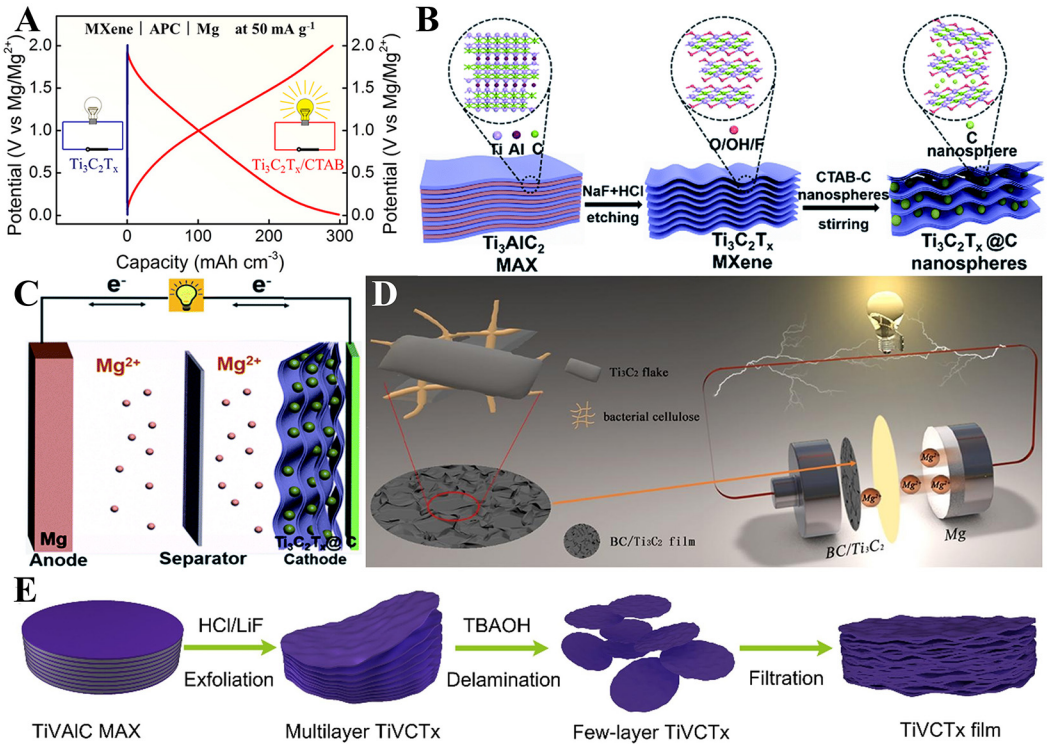

Figure 8. (A) GCD curves of the $Ti_3C_2T_x$/CTAB and $Ti_3C_2T_x$. This figure is quoted with permission from Xu *et al.* Copyright (2018) American Chemical Society[53]. (B) Schematic illustration of the synthesis process of $Ti_3C_2T_x$@C. (C) Schematic illustration of the Mg//$Ti_3C_2T_x$@C battery. This figure is quoted with permission from Liu *et al.* Copyright (2019) Royal Society of Chemistry[78]. (D) Schematic illustration of the Mg// BC/Ti_3C_2 battery. This figure is quoted with permission from Zhu *et al.* Copyright (2020) Elsevier[79]. (E) Schematic illustration of the synthesis process of $TiVCT_x$. This figure is quoted with permission from Zhang *et al.* Copyright (2024) Elsevier[80].

nanospheres [Figure 8B][78]. The BET surface area results showed that $Ti_3C_2T_x$@C exposed more surface area (103.8 $m^2 g^{-1}$) than pure $Ti_3C_2T_x$ (12.7 $m^2 g^{-1}$), which further verified that carbon nanospheres can alleviate the restacking of MXene. For $Ti_3C_2T_x$@C, the (002) peak shifted to a lower angle than that of $Ti_3C_2T_x$. Thus, the intercalation of carbon nanospheres can expand the layer spacing of MXene, resulting in more active sites and diffusion paths for the Mg^{2+} ions. Therefore, the electrode had excellent Mg-ion storage ability (198.7 mA h g^{-1} at 0.01 A g^{-1} and 123.3 mA h g^{-1} at 0.2 A g^{-1}) [Figure 8C]. In addition to expanding the interlayer spacing, processing 2D MXene nanosheets into 3D structures is an effective strategy for enhancing the electrochemical performance of MXenes. The 3D conductive Ti_3C_2 networks were prepared by introducing bacterial celluloses (BC) into MXenes to synthesize a flexible freestanding BC/Ti_3C_2 film [Figure 8D][79]. XRD and DFT confirmed that the introduced BC not only increased the layer spacing but also promoted Mg-ion migration. The galvanostatic intermittent titration technique (GITT) curves revealed that BC/Ti_3C_2 had faster Mg^{2+} ion diffusion than the pure Ti_3C_2 film. Therefore, BC/Ti_3C_2 delivered a discharge capacity of 171 mA h g^{-1} at 0.05 A g^{-1} and 88% capacity retention after 100 cycles. Therefore, appropriate modifications are necessary to use MXenes as cathode materials for MIBs.

In addition to monometallic MXenes, bimetallic MXenes have also been investigated as energy-storage materials. Bimetallic MXenes utilize bimetallic elements at the M site and exhibit various advantages[80]. $TiVCT_x$ MXene not only combines the advantages of the high reducibility of V-based MXene and the high stability of Ti-based MXene, but also exhibits fewer atomic layers and higher conductivity. The synthesis process of $TiVCT_x$ is shown in Figure 8E. Therefore, when $TiVCT_x$ is directly used as a cathode without

conductive additives, binders, and collectors[80], the $TiVCT_x$ film exhibits a high specific capacity (111 mA h g^{-1} at 0.05 A g^{-1}) and excellent cyclic stability (over 1,000 cycles at 0.5 A g^{-1}). *Ex-situ* XRD, X-ray photoelectron spectroscopy (XPS), and high-resolution transmission electron microscopy (HRTEM) characterization demonstrate a reversible Mg^{2+} insertion/extraction mechanism. At present, there is little research in the field of bimetallic MXenes, and there are more bimetallic MXenes to be explored in the future. The electrochemical properties of MXenes and their derivatives as cathodes are summarized in Table 1[34,53,61-63,66,67,73,75,78-80].

MXene/transition metal oxide composites as cathodes

Manganese oxide as cathodes

Manganese (Mn)-based materials are extensively utilized in energy-storage devices because they offer advantages such as low cost, environmental friendliness, abundant reserves, and high theoretical capacity/voltage[81]. As a transition metal, Mn is abundant in oxidation valence states (bivalent, trivalent, and quadrivalent) and exists in a variety of Mn-based oxides, such as MnO_2, MnO, Mn_2O_3, Mn_3O_4, and $ZnMn_2O_4$. Among these, MnO_2 has received the most attention. The basic structural unit of MnO_2 is the MnO_6 octahedron, which can form different structures such as chains, tunnels, and layers by sharing angles/edges, resulting in different MnO_2 phases[82]. The structures of MnO_2 materials with different crystals are shown in Figure 9. Unfortunately, Mn-based oxides used as cathodes suffer from issues such as active material dissolution, poor conductivity, and irreversible phase transitions, leading to limited cycle life and fast capacity decay[83]. Zhao *et al.* reported that pure MnO_2 exhibited an initial capacity of 270 mA h g^{-1} at 200 mA g^{-1}, which only remained at 80 mAh g^{-1} after 60 cycles in ZIBs[84]. The combination of MXenes with Mn oxides can significantly enhance the conductivity of the material, accelerate the electron transfer rates, and improve electrochemical performance. Furthermore, MXenes with hydrophilic groups can effectively boost the wettability of the cathode toward aqueous electrolytes, thereby reducing the interfacial transfer resistance.

MXene/manganese oxide composites as cathodes in ZIBs

MnO_2 is the most studied Mn-based compound, and its composite with MXenes can take various forms, such as MnO_2 particles grown on the surface of MXenes and the assembly of MnO_2 nanosheets and MXene sheets by electrostatic interactions. MXenes act as a framework to ensure fast electron transfer, and the Mn dioxide provides a high capacity. Therefore, the composite material exhibits better electrochemical properties. K-V_2C@MnO_2 composites are obtained by alkalizing V_2CT_x MXenes (K-V_2C) with KOH and growing MnO_2 *in situ* on K-V_2C using the hydrothermal method [Figure 10A][85]. The K-V_2C with inserted K^+ can be used as the nucleation site of MnO_2 in hydrothermal processes; meanwhile, the insertion of K^+ increases the layer spacing of MXenes. An SEM image of K-V_2C@MnO_2 [Figure 10B and C] shows that the formed MnO_2 grows uniformly on the K-V_2C surface. XRD patterns show that the formed MnO_2 is in the δ-MnO_2 phase (JCPDS No.80-1098). The layered V_2CT_x framework with high conductivity facilitates electron transport, effectively preventing the volume change of MnO_2, inhibiting the dissolution of MnO_2 and reducing the loss of the active material during charging and discharging. Correspondingly, the uniformly grown MnO_2 nanosheets on the V_2CT_x framework increase the specific surface area, ensuring sufficient active sites to enhance the reaction kinetics and increase the capacity. In addition, the alkalization treatment also transforms the -F group into a hydrophilic -OH group, which accelerates the wettability of the electrolyte to the cathode[86]. Based on the above characteristics, the discharge capacity of the K-V_2C@MnO_2 cathode at 0.3 A g^{-1} is 408.1 mA h g^{-1}. Even at 10 A g^{-1}, the cathode maintains a discharge capacity of 119.2 mA h g^{-1} after 10,000 cycles.

Table 1. Summary of the electrochemical properties of MXenes and their derivatives as cathodes

Battery system	Cathode materials	Capacity	Cycle stability	Ref.
ZIBs	alk-V_2CT_x	498.2 mA h g^{-1} at 0.1 A g^{-1}	96.2% after 20,000 cycles at 10 A g^{-1}	[34]
	$Ti_3C_2Br_2$	97.6 mA h g^{-1} at 0.5 A g^{-1}	80% after 1,000 cycles at 4 A g^{-1}	[61]
	$Ti_3C_2I_2$	135 mA h g^{-1} at 0.5 A g^{-1}	80% after 700 cycles at 4 A g^{-1}	[61]
	1.8-V_2CT_x	358 mA h g^{-1} at 30 A g^{-1}	81.4% after 2,000 cycles at 30 A g^{-1}	[62]
	V_2AlC	409.7 mA h g^{-1} at 0.5 A g^{-1}	/	[63]
	MVO@VC	287.6 mA h g^{-1} at 10 A g^{-1}	92.9% after 25,000 cycles at 10 A g^{-1}	[66]
	VSe_2@V_2CT_x	231.3 mA h g^{-1} at 0.5 A g^{-1}	93.1% after 600 cycles at 2.0 A g^{-1}	[67]
AIBs	TBAOH-FL-V_2CT_x	300 mA h g^{-1} at 0.1 A g^{-1}	42.1% after 100 cycles at 0.2 A g^{-1}	[75]
	C-Nb_2CT_x	108 mA h g^{-1} at 0.2 A g^{-1}	80% after 500 cycles at 0.5 A g^{-1}	[73]
MIBs	CTAB-Ti_3C_2	300 mA h cm^{-3} at 0.05 A g^{-1}	63.1% after 250 cycles at 0.2 A g^{-1}	[53]
	$Ti_3C_2T_x$@C	198.7 mA h g^{-1} at 0.01 A g^{1}	85% after 400 cycles at 0.05 A g^{-1}	[78]
	BC/Ti_3C_2	171 mA h g^{-1} at 0.05 A g^{-1}	88% after 100 cycles at 0.05 A g^{-1}	[79]
	TiVCT$_x$	111 mA h g 1 at 0.05 A g^{1}	64.8% after 1,000 cycles at 0.5 A g^{-1}	[80]

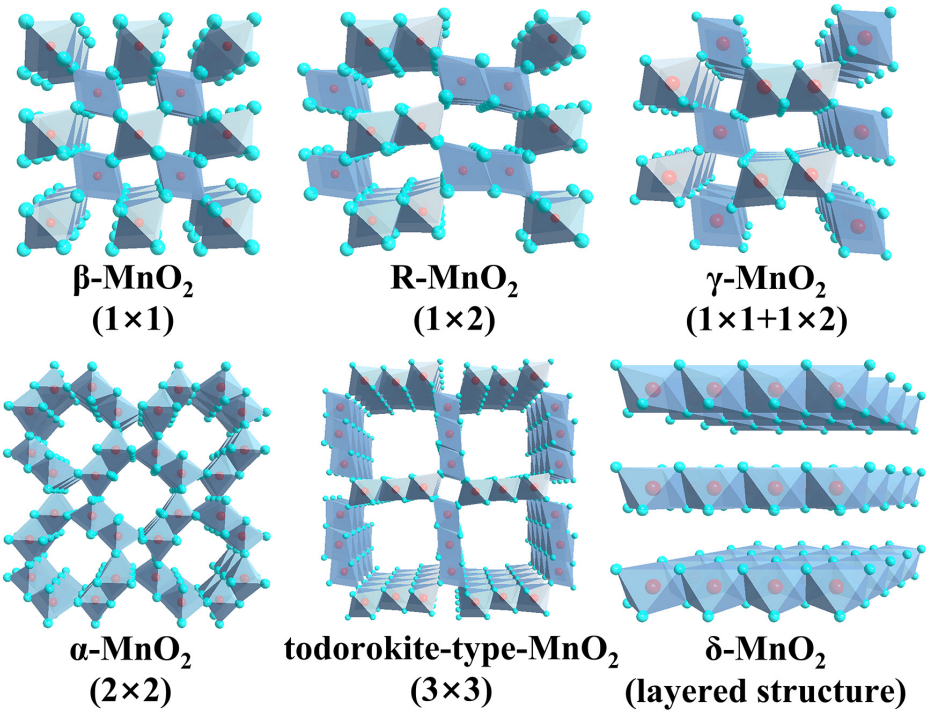

Figure 9. The structures of MnO_2 with different crystals.

In contrast to the above-mentioned Mn dioxide particles grown on layered MXenes, a 2D MnO_2/MXene superlattice was synthesized using the solution-phase assembly method [Figure 10D][87]. The 2D MnO_2/MXene superlattice consisted of unilamellar MnO_2 and MXene nanosheets that stacked alternately [Figure 10E]. The high conductivity of the MXene nanosheets promoted electron transport while preventing the aggregation of MnO_2 nanosheets and enhancing their structural stability. Moreover, the regular stacking of the 2D MnO_2/MXenes exposed sufficient active sites and promoted ion transport. In addition to the common hydrothermal and electrostatic self-assembly methods, Shi *et al.* designed a new type of 3D microflower-like MXene-MnO_2 material combined with spray-drying technology [Figure 10F][88]. In this material ($Ti_3C_2T_x$@MnO_2), MnO_2 nanoparticles were encapsulated in pleated MXene nanosheets.

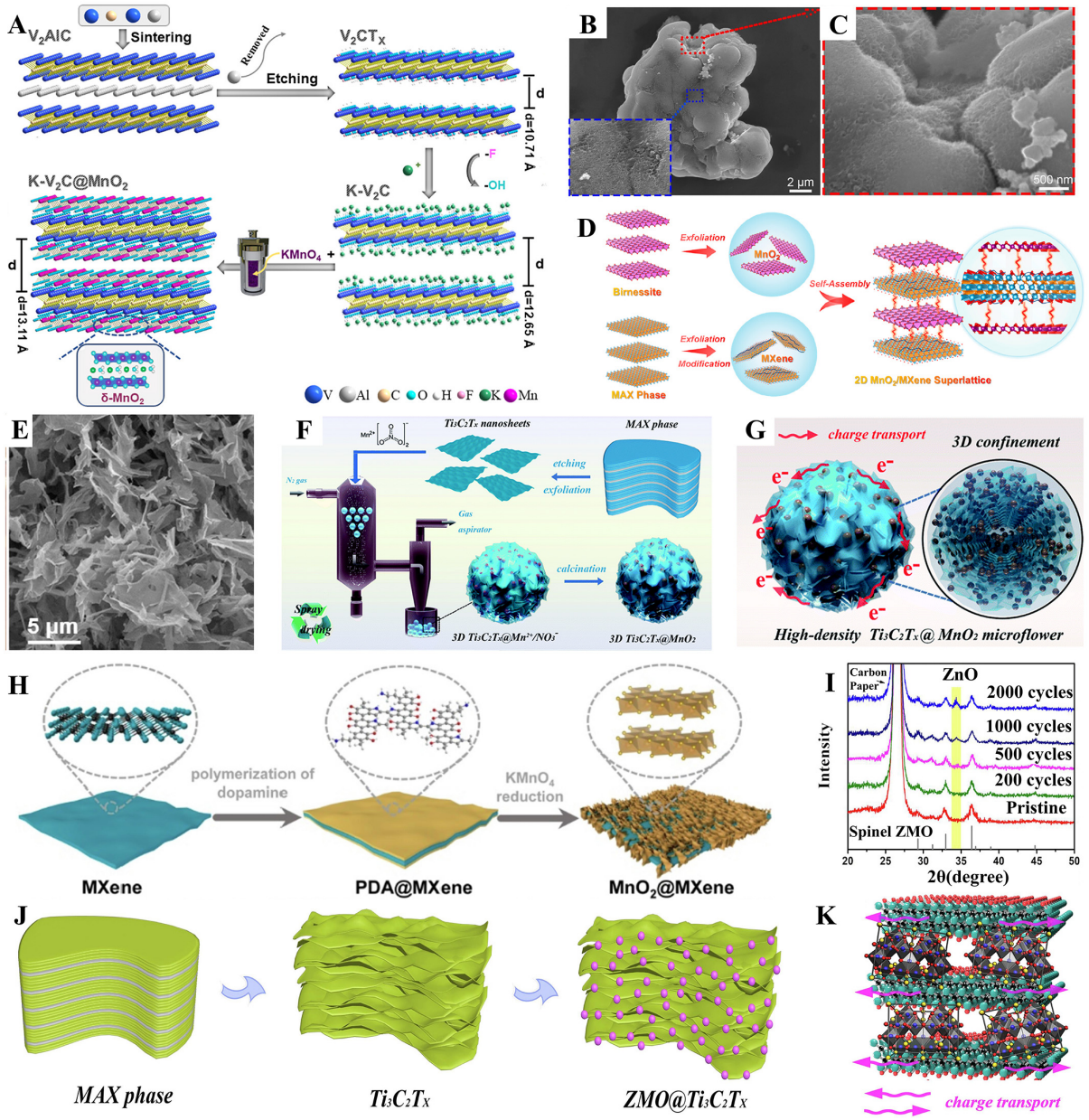

Figure 10. (A) Schematic representation of the preparation of K-V_2C@MnO_2. (B and C) SEM image of K-V_2C@MnO_2. This figure is quoted with permission from Zhu *et al.* Copyright (2021) American Chemical Society[85]. (D) Schematic representation of the preparation process of the MnO_2/MXene superlattice. (E) SEM image of the MnO_2/MXene. This figure is quoted with permission from Wang *et al.* Copyright (2023) American Chemical Society[87]. (F) Schematic representation for the synthesis strategy of 3D $Ti_3C_2T_x$@MnO_2 microflowers. (G) Schematic representation of the mechanism of improved performance of 3D high-density $Ti_3C_2T_x$@MnO_2 microflower cathode. This figure is quoted with permission from Shi *et al.* Copyright (2020) Royal Society of Chemistry[88]. (H) Schematic representation of the synthetic process for MnO_2@MXene heteronanosheets. This figure is quoted with permission from Wu *et al.* Copyright (2023) Elsevier[89]. (I) The *ex-situ* XRD pattern of inactive ZnO byproduct generated during the cycles of ZMO cathode. (J) Schematic representation of the synthesis of ZMO@$Ti_3C_2T_x$ composite. (K) Schematic diagram of ZMO@$Ti_3C_2T_x$ cathode accelerating charge transfer during charging and discharging. This figure is quoted with permission from Shi *et al.* Copyright (2020) Elsevier[90].

The electrochemical behavior of the $Ti_3C_2T_x$@MnO_2 cathode in aqueous solution is shown in Figure 10G. The highly conductive $Ti_3C_2T_x$ nanosheets provided continuous and interconnected electron transmission

paths, facilitating charge transport (red arrow), and the rich functional groups of the $Ti_3C_2T_x$ nanosheets enhanced the hydrophilicity of the electrode. In addition, the black circle in Figure 10G represents a stable skeleton that prevents structural collapse. The MnO_2 nanoparticles were wrapped by MXene nanosheets, suppressing the aggregation of MnO_2 nanoparticles and the dissolution of Mn^{2+}. The 3D MXene@MnO_2 microflower cathode had a capacity of 301.2 mA h g^{-1} at 0.1 A g^{-1} and could undergo 2,000 cycles at 0.5 A g^{-1}. When the cathode reached 8.0 mg cm^{-2}, it still had a large capacity of 287.6 mA h g^{-1} at 0.1 A g^{-1}.

MXenes can be used not only for aqueous ZIBs but also for non-aqueous ZIBs. The 2D δ-MnO_2@MXene heteronanosheets were obtained by deposition of δ-MnO_2 nanosheets on MXene [Figure 10H][89]. The deposition was achieved through a chemical reaction between $KMnO_4$ and polydopamine (PDA). In 0.5 M Zn triflate [$Zn(OTf)_2$] in triethyl phosphate (TEP) organic electrolytes, the MnO_2@MXene heteronanosheet exhibited only Zn^{2+} insertion and no H^+ insertion, which avoided byproduct formation, Mn shuttling effects, and structural damage. At 10.5 mg cm^{-2}, the MnO_2@MXene heteronanosheet cathode achieved an areal capacity of 1.9 mAh cm^{-2}. In addition to layered Mn dioxide, $ZnMn_2O_4$ spinel (ZMO) is also a promising energy-storage material. However, during charging and discharging, ZMO is transformed into MnO_2. This transformation leads to the degradation of the spinel structure and the formation of irreversible inactive ZnO byproducts, resulting in poor cycling stability [Figure 10I][90]. Based on the above challenges, ZMO nanoparticles were assembled on $Ti_3C_2T_x$ MXene sheets via a hydrothermal process to synthesize a ZMO@$Ti_3C_2T_x$ composite. As shown in Figure 10J, a large number of ZMO nanoparticles were immobilized on the $Ti_3C_2T_x$ framework, which provided a higher capacity for the cathode, whereas the $Ti_3C_2T_x$ framework stabilized the structure and accelerated electron transport [Figure 10K]. The ZMO@$Ti_3C_2T_x$ composite cathode exhibited a capacity of 172.6 mA h g^{-1} at 0.1 A g^{-1}, with a capacity retention of 92.4% after 5,000 cycles at 1 A g^{-1}.

Vanadium oxide as cathodes

V has a variety of valence states, and V-based materials have high theoretical capacities and superior rate performances as cathodes[91-94]. The constituent units of the V-O coordination polyhedron include tetrahedrons, triangular bipyramids, and square pyramids, and these units can change according to the oxidation state of V. Consequently, numerous V oxides can be constructed by sharing the angles and/or edges of the polyhedra. However, the main challenge in V-based materials is capacity decay owing to structural damage and the dissolution of cathodes. $V_2O_5{\cdot}nH_2O$ was reported to have an initial capacity of 273.9 mA h g^{-1} and retain less than 100 mA h g^{-1} after 20 cycles in ZIBs, indicating fast capacity decay[95]. The heterogeneous interface formed by the composite of V oxide and MXene facilitated rapid electron and ion transfer, thereby enhancing the electrochemical kinetics. Furthermore, the composite exhibited remarkable energy-storage capabilities at low temperatures.

MXene/vanadium oxide composites as cathodes in ZIBs

V-based oxides are ideal candidates for ZIB cathodes due to their multielectron transfer mechanism and large layer spacing, which are favorable for ion transport[96,97]. Designing V oxides and MXenes into heterostructures is a promising strategy for enhancing charge transport. As illustrated in Figure 11, the difference in the energy bands creates a built-in electric field within the heterostructure, facilitating electron transfer and ion diffusion. Zhang *et al.* prepared layer-stacked MVO + V_2C heterostructures by electrostatic self-assembly using $Mn_xV_2O_6$ (MVO) nanobelts and V_2C [Figure 12A], which was used as a cathode in ZIBs operating at a wide-temperature range of -20-40 °C[98]. Many nanochannels and built-in electric fields between the interstacked $Mn_xV_2O_6$ and V_2CT_x achieve rapid Zn^{2+} transport and improve the intrinsic conductivity and reaction kinetics. Furthermore, the presence of numerous nanochannel interlayers enhances the wettability of the electrolyte, thereby facilitating access to the electrodes. The cycling

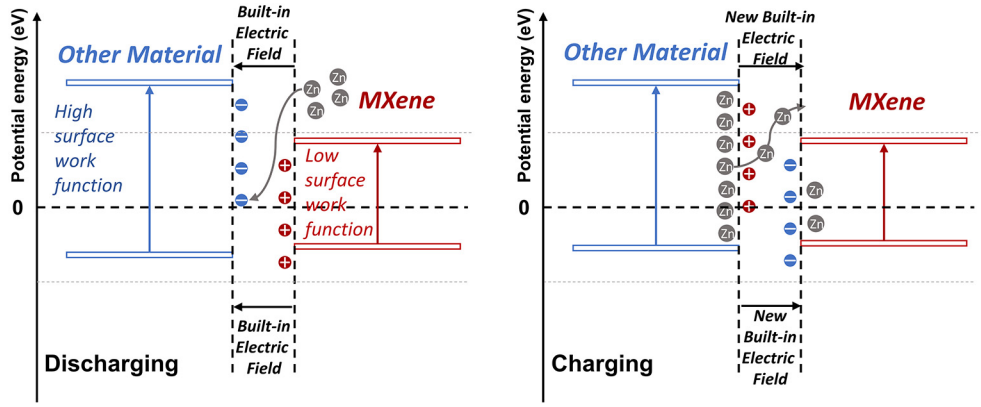

Figure 11. Schematic of the built-in electric field formed by MXene and other materials.

performance of the MVO + V_2C cathode at -20 °C was tested [Figure 12B], and the results showed that the MVO + V_2C cathode had a discharge capacity of 301.3 mA h g^{-1} at 0.5 A g^{-1}, confirming that the MXene-based heterostructure endows ZIBs with excellent performance at a wide temperature range.

In addition to $Mn_xV_2O_6$, $H_2V_3O_8$ nanowires have been utilized to construct a built-in electric field with MXenes to promote ion transfer. The average valence of V in $H_2V_3O_8$ is 4.67, and high-valence V can accommodate a large number of Zn ions[99]. $H_2V_3O_8/Ti_3C_2T_x$ was prepared using a one-step hydrothermal method, and the surface of delaminated $Ti_3C_2T_x$ was uniformly covered with $H_2V_3O_8$ nanowires [Figure 12C][100]. The $H_2V_3O_8$ nanowires provided more active sites, whereas the MXene nanosheets increased the conductivity and ensured structural stability. The DFT calculations further revealed that the built-in electric field at the $H_2V_3O_8$/MXene interface induced outstanding Zn-ion diffusion kinetics and superior Zn storage capacity, which is consistent with the results shown in Figure 11. Therefore, the $H_2V_3O_8$/MXene electrode achieves a capacity of 437.3 mA h g^{-1} at 5.0 A g^{-1} and maintains structural stability over 9,000 cycles at 10 A g^{-1}. In addition, the 2D heterogeneous structure (2D HVO@Ti_3C_2) can also be constructed by combining $V_5O_{12}·6H_2O$ nanosheets (HVO) with Ti_3C_2 nanosheets through electrostatic self-assembly [Figure 12D][101]. The researchers discovered 2D dynamic heterogeneous interface coupling; the O-Ti bonds in the interfacial V-O-Ti bonds of the 2D HVO@Ti_3C_2 cathode were reversibly broken and rebuilt during cycling. As shown in Figure 12E, during charging and discharging, owing to the built-in electric field formed by Ti_3C_2 and HVO, the heterogeneous interface enabled electrons to be reversibly transferred to the Ti_3C_2 layers through the V-O-Ti heterogeneous interface bonds, which increased the electron transfer pathway and improved the reaction kinetics. Consequently, the 2D HVO@Ti_3C_2 enhanced the capacity of the cathode (457.1 mA h g^{-1} at 0.2 A g^{-1}).

V_2O_5, a classical V oxide, has also been combined with MXenes to form a built-in electric field. V_2O_5 nanoplates with $Ti_3C_2T_x$ MXene layers (VPMX) were assembled using van der Waals forces [Figure 12F][102]. Compared to the V_2O_5 cathode, MXene coated on the surface of V_2O_5 inhibited the dissolution of V and enhanced the structural stability of the VPMX cathode during charging and discharging [Figure 12G]. As shown in Figure 11, the heterogeneous interface between V_2O_5 and MXene allowed rapid electron transfer and improved the bulk electrochemical kinetics. Additionally, the water molecules in the VPMX cathode weakened the electrostatic interactions between the cathode and Zn^{2+}, accelerating ion transport and stabilizing the structure. The VPMX cathode achieved a capacity of 243.6 mA h g^{-1} at 5.0 A g^{-1} and a long cycling life of over 5,000 cycles at 10 A g^{-1}.

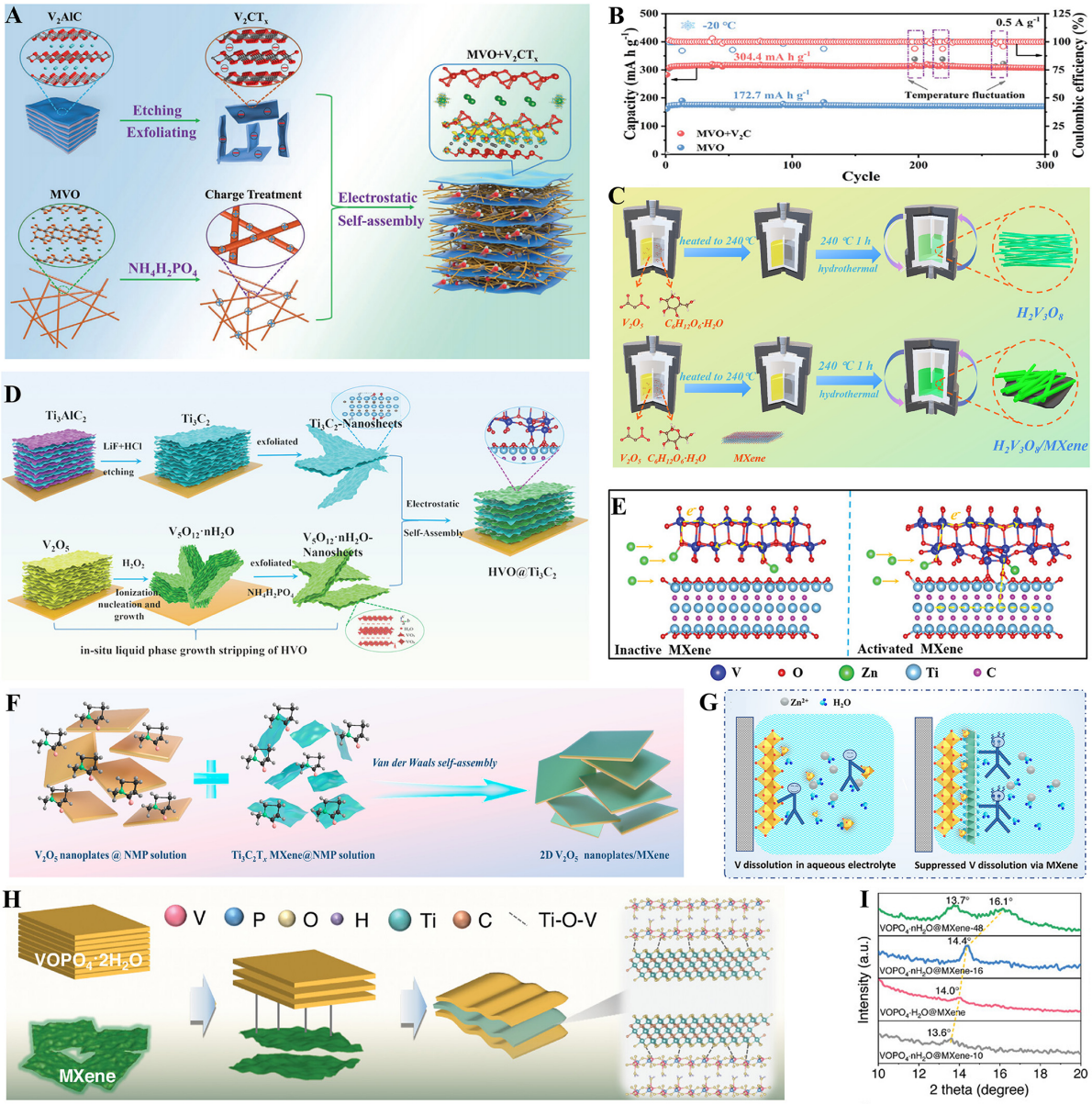

Figure 12. (A) Schematic of the preparation process of MVO + V_2C heterostructures. (B) Cycle performance of MVO + V_2C cathode at -20 °C (0.5 A g^{-1}). This figure is quoted with permission from Zhang *et al.* Copyright (2024) John Wiley and Sons[98]. (C) Schematic of the preparation of $H_2V_3O_8$ and $H_2V_3O_8$/MXene. This figure is quoted with permission from Liang *et al.* Copyright (2022) Elsevier[100]. (D) Preparation process of HVO@Ti_3C_2 2D heterostructure material. (E) Schematic representation of the insertion of Zn^{2+} into the HVO-Ti_3C_2 (left) and HVO@Ti_3C_2 (right) cathodes. This figure is quoted with permission from Xiao *et al.* Copyright (2023) John Wiley and Sons[101]. (F) Schematic of the assembly process of V_2O_5 nanoplates and $Ti_3C_2T_x$ MXene. (G) Schematic diagram of the dissolution of V in V_2O_5 nanoplates cathode and the inhibition of V dissolution in V_2O_5 nanoplates/MXene hybrid cathode in aqueous electrolyte. This figure is quoted with permission from Liu *et al.* Copyright (2022) American Chemical Society[102]. (H) Schematic representation for the synthetic process of $VOPO_4{\cdot}nH_2O$@MXene composite. (I) The XRD patterns of $VOPO_4{\cdot}nH_2O$@MXene composites with different MXene content. This figure is quoted with permission from Zheng *et al.* Copyright (2023) John Wiley and Sons[103].

MXene/vanadium oxide composites as cathodes in AIBs

In addition to serving as a framework, the numerous functional groups on the MXene surface allow it to interact with other materials via the formation of M-O-Ti (M = metal atoms) and hydrogen bonds. Studies using the M-O-Ti bonds formed between $VOPO_4$-$2H_2O$ and MXene to exfoliate nanosheets and obtain

$VOPO_4$-nH_2O with different water contents have been reported. A $VOPO_4 \cdot nH_2O$@MXene composite was prepared by mechanical stirring to mix $VOPO_4 \cdot 2H_2O$ with different MXene contents (10%, 12%, 16%, and 48%) [Figure 12H][103]. The XRD patterns [Figure 12I] showed that with an increase in MXene, the (001) peak moved to a higher degree, and the number of water molecules in the $VOPO_4$-$2H_2O$ interlayer was reduced, indicating that the force between MXene and $VOPO_4$-$2H_2O$ affects the number of water molecules in the $VOPO_4$-$2H_2O$ interlayer. The $VOPO_4$-H_2O@MXene composite with 12% MXene exhibited the best electrochemical properties among all MXene contents. The $VOPO_4$-H_2O@MXene cathode achieved a discharge capacity of 329.6 mA h g^{-1} at 1 A g^{-1} and a long cycling life of over 2,000 cycles at 1 A g^{-1} without capacity loss. The electrochemical properties of MXene/transition metal oxide composites as cathodes are summarized in Table 2[85,87-90,98,100-103].

MXene/sulfur-based material composites as cathodes

Sulfur-based material as cathodes

Sulfur is a lightweight, environmentally friendly element that is abundant on Earth, and sulfur cathodes have a high theoretical capacity (1,675 mA h g^{-1})[104]. Therefore, sulfur conversion cathodes offer high energy density, cost-effectiveness, and environmental friendliness and can be used in MMIBs. Except for sulfur cathodes, metal sulfides have the advantages of tunable layer spacing and high polarizability. Therefore, metal sulfides are promising candidate cathode materials for MMIBs. Sulfur atoms have a lower electronegativity than oxygen atoms, and the electrostatic interaction between the inserted multivalent ions and metal sulfides is smaller, which helps the electrode structure to remain stable. Metal sulfides, such as Mo_6S[105], Co_9S_8[106], MoS_2, WS_2, VS_2, and VS_4, have been used to investigate cathodes[107]. However, sulfur cathodes face challenges such as active material polysulfide dissolution in the electrolyte and sluggish polysulfide transformation kinetics. The development of metal sulfides is hindered by their poor electrical conductivities, which are detrimental to ion transport. For example, pure MoS_2 delivers a capacity of only 62 mA h g^{-1} at 0.5 A g^{-1} in MIBs[108]. The combination of MXenes with sulfur-based materials has been shown to reduce the shuttle effect of sulfur and facilitate the diffusion of metal ions. Furthermore, the large specific surface area of MXenes allows sulfides to expose more active sites in the composites, thereby enhancing the cathode capacity.

MXene/sulfur-based material composites as cathodes in ZIBs

Since the electronegativity of S^{2-} is lower than that of O^{2-}, V-based sulfide cathodes have a weaker electrostatic interaction with the bivalent Zn^{2+} than that of V-based oxide cathodes, thus allowing faster ion diffusion. As a promising cathode candidate for ZIBs, layered VS_2 has a large layer spacing and abundant V redox chemical properties. However, the relatively low electrical conductivity and severe agglomeration of VS_2 nanosheets deteriorate their electrochemical performance. A new 3D interconnected $VS_2 \perp V_4C_3T_x$ heterostructural material was prepared using the solvothermal method [Figure 13A][109]. VS_2 nanosheets were uniformly distributed on the surface of the $V_4C_3T_x$ MXene framework, and this framework improved the conductivity of the cathode. Simultaneously, MXene effectively suppressed the volume change of VS_2. Thus, the use of VS_2 nanosheets as active materials contributes to their high capacity. Moreover, $V_4C_3T_x$ MXene is used as a Zn anode coating, which inhibits the growth of Zn dendrites during cycling[110] and provides the anode with a more uniform electric field distribution[111]. The $V_4C_3T_x$@Zn symmetrical battery showed excellent cycling stability for approximately 1,700 h at 1 mA cm^{-2}. The full cell was assembled with the $VS_2 \perp V_4C_3T_x$ heterostructural material as the cathode and Zn foil with a protective layer of $V_4C_3T_x$ MXene on the surface as the anode [Figure 13B]. The $VS_2 \perp V_4C_3T_x || V_4C_3T_x$@Zn battery had a capacity of 157.1 mA h g^{-1} after 5,000 cycles at 5 A g^{-1}.

Table 2. Summary of the electrochemical properties of MXene/transition metal oxide composites as cathodes

Battery system	Cathode materials	Capacity	Cycle stability	Ref.
ZIBs	K-V_2C@MnO_2	408.1 mA h g^{-1} at 0.3 A g^{-1}	99.1% after 10,000 cycles at 10 A g^{-1}	[85]
	MnO_2/MXene	315.1 mA h g^{-1} at 0.2 A g^{-1}	88.1% after 5,000 cycles at 5 A g^{-1}	[87]
	$Ti_3C_2T_x$@MnO_2	301.2 mA h g^{-1} at 0.1 A g^{-1}	90.6% after 2,000 cycles at 0.5 A g^{-1}	[88]
	δ-MnO_2@MXene	163 mA h g^{-1} at 0.1 A g^{-1}	84.5% after 1,000 cycles at 0.1 A g^{-1}	[89]
	ZMO@$Ti_3C_2T_x$	172.6 mA h g^{-1} at 0.1 A g^{-1}	92.4% after 5,000 cycles at 1 A g^{-1}	[90]
ZIBs	MVO + V_2C	301.3 mA h g^{-1} at 0.5 A g^{-1} (-20 °C)	100% after 300 cycles at 0.5 A g^{-1}	[98]
	MVO + V_2C	301.3 mA h g^{-1} at 0.5 A g^{-1} (40 °C)	100% after 120 cycles at 0.5 A g^{-1}	[98]
	$H_2V_3O_8$/MXene	437.3 mA h g^{-1} at 3.0 A g^{-1}	76.9% after 9,000 cycles at 10 A g^{-1}	[100]
	2D HVO@Ti_3C_2	457.1 mA h g^{-1} at 0.2 A g^{-1}	88.9% after 1,000 cycles at 5 A g^{-1}	[101]
	VPMX73	402.5 mA h g^{-1} at 0.2 A g^{-1}	99.5% after 5,000 cycles at 10 A g^{-1}	[102]
	VPMX73	402.5 mA h g^{-1} at 0.2 A g^{-1}	99.5% after 5,000 cycles at 10 A g^{-1}	[102]
AIBs	$VOPO_4$-H_2O@MXene	329.6 mA h g^{-1} at 1 A g^{-1}	100% after 2,000 cycles at 1 A g^{-1}	[103]

MXene/sulfur-based material composites as cathodes in AIBs

Metal-sulfide/MXene composites have also been used as cathodes for AIBs. Encapsulating the active material particles with MXenes can reduce the loss of the active material and inhibit the aggregation of nanoparticles, thereby ensuring sufficient active sites and improving the electrochemical performance of the composite cathode. The synthesis of a new type of cobalt (Co) sulfide nanoparticles/MXene composite is shown in Figure 13C[112]. In the first step, a spongy 3D precursor of ZIF-67 encapsulated in an interlayer of MXene was prepared by *in-situ* growth and self-assembly. In the second step, the ZIF-67@MXene precursor and an appropriate amount of S powder were annealed at high temperatures. After carbonization and vulcanization, a 3D MXene-wrapped Co sulfide nanoparticle composite embedded in a hollow carbon nanobox (Co_9S_8 NP@NPC@MXene) was prepared. Compared to the Co_9S_8 NP@NPC composite, Co_9S_8 NP@NPC@MXene had a more stable structure. Moreover, the MXene layers in Co_9S_8 NP@NPC@MXene effectively reduced the dissolution of Co_9S_8 nanoparticles and inhibited their aggregation and overgrowth, which contributed to high capacity maintenance [Figure 13D]. The Co_9S_8 NP@NPC@MXene cathode had a capacity of 277 mA h g^{-1} after 100 cycles at 0.1 A g^{-1} and 110 mA h g^{-1} after 1,000 cycles at 1 A g^{-1}.

MXene/sulfur-based material composite as cathode in MIBs

Sulfur is an ideal cathode material owing to its abundance, cost-effectiveness, and high theoretical capacity[113]. Nevertheless, sulfur faces various challenges, such as poor electrical conductivity, slow electron and ion transport, and polysulfide shuttling[114]. MXenes with high electronic conductivities and rich termination groups have been demonstrated to effectively increase sulfur utilization[115]. Therefore, the combination of sulfur and MXenes can effectively exert synergistic effects on both materials. MXenes as sulfur host materials in Mg-S batteries were first reported in 2021[116]. The S_8-sandwich cathode is composed of $Ti_3C_2T_x$, carbon nanotubes (CNT) and S_8 nanoparticles through low-temperature vacuum-filtration methods without a current collector or binder. Notably, as shown in Figure 14A, the S_8-sandwich is a sandwich-like architecture, where MXene acts as an interlayer with a mixed cathode of S_8 and CNT. S_8, as the source of redox-active sulfur, makes a major contribution to the capacity; CNT plays a critical role in the formation of the conductive network, and MXene with polar termination groups reduces sulfur shuttle and confines the sulfur species. The GCD curves demonstrate that the MXene interlayer significantly improves the capacity and average voltage. Therefore, MXene increases the discharge capacity of the electrode material from 290 to 530 mA h g^{-1}, with 83% capacity retention over 25 cycles. Furthermore, a Ti_3C_2@CoO heterostructure was synthesized as sulfur hosts via a self-assembly and annealing process[117]. DFT confirms that CoO can guarantee more Mg polysulfide adsorption during the cycle, and Ti_3C_2 is favorable for Mg-ion

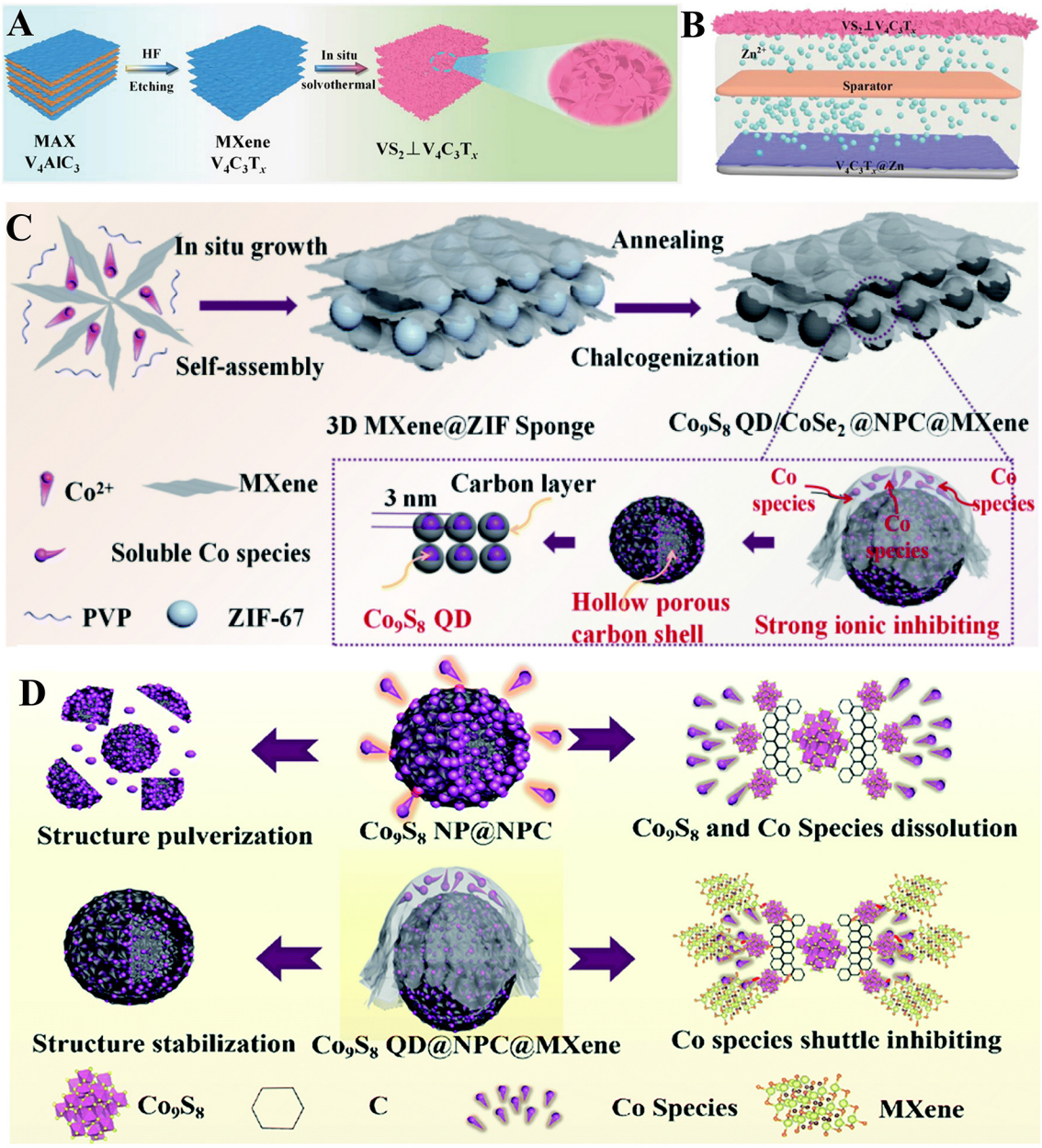

Figure 13. (A) Schematic diagram for the preparation for the $VS_2 \perp V_4C_3T_x$ material. (B) The schematic diagram of the $VS_2 \perp V_4C_3T_x$||$V_4C_3T_x$@Zn full cell. This figure is quoted with permission from Mao *et al.* Copyright (2023) John Wiley and Sons[109]. (C) Schematic representation for the preparation of Co_9S_8 NP@NPC@MXene. (D) The schematic representation of the performance enhancement of the Co_9S_8 NP@NPC@MXene. This figure is quoted with permission from Yao *et al.* Copyright (2021) Royal Society of Chemistry[112].

diffusion [Figure 14B]. Batteries were assembled using S-Ti_3C_2@CoO as the cathode, Mg foils as the anode, and 1 M $Mg(TFSI)_2/AlCl_3$/diglyme as the electrolyte. The battery exhibited an excellent capacity of 540 mA h g^{-1} at 100 mA g^{-1} over 70 cycles. This study provides insight into MXene-based materials as sulfur host materials.

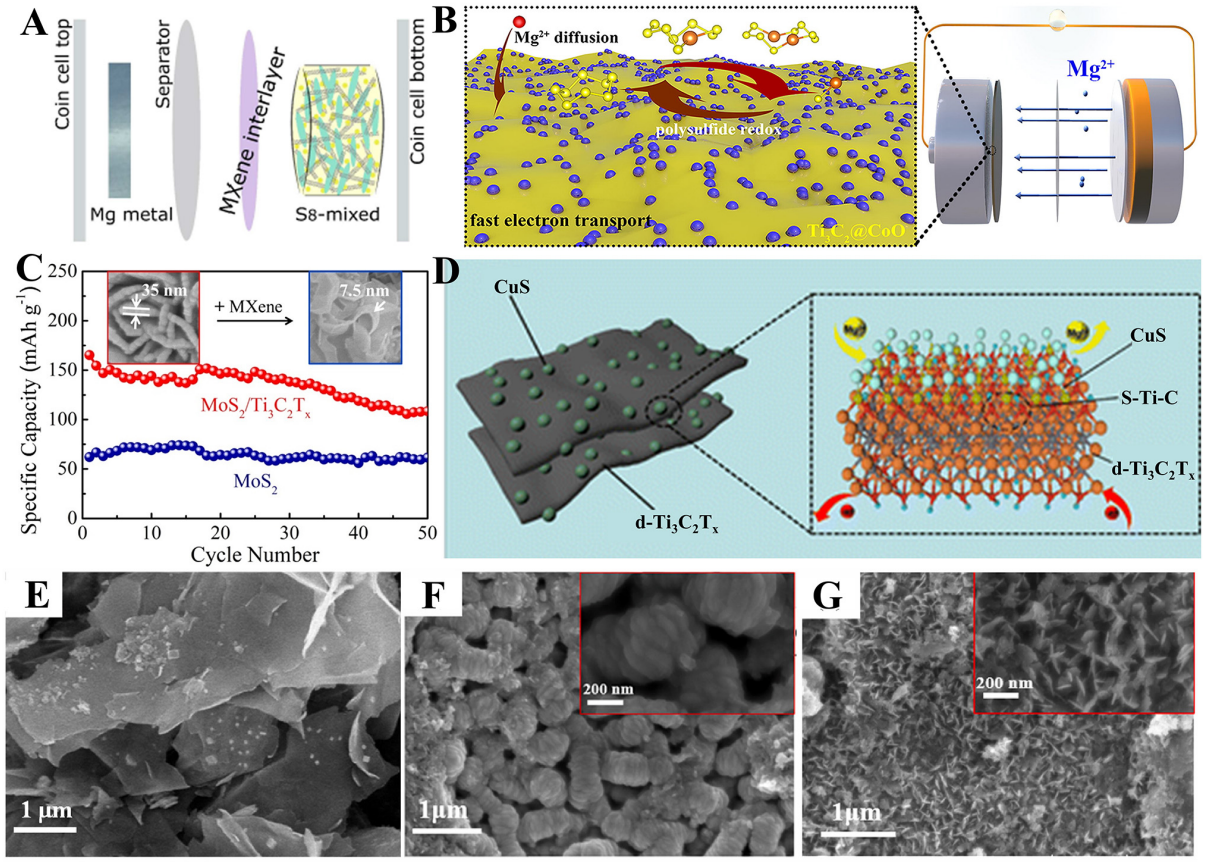

Figure 14. (A) Schematic illustration of S_8-mixed cathode. This figure is quoted with permission from Kaland *et al.* Copyright (2021) John Wiley and Sons[116]. (B) Schematic diagram of magnesium polysulfide redox mechanism of the S-Ti_3C_2@CoO electrode. This figure is quoted with permission from Xu *et al.* Copyright (2022) Elsevier[117]. (C) Cycle performance and SEM image of $MoS_2/Ti_3C_2T_x$. This figure is quoted with permission from Xu *et al.* Copyright (2018) Elsevier[108]. (D) Schematic illustration of CuS/d-Ti_3C_2Tx structure. This figure is quoted with permission from Cheng *et al.* Copyright (2023) Royal Society of Chemistry[118]. SEM images of (E) Ti_3C_2, (F) VS_4 and (G) VS_4@Ti_3C_2/C. This figure is quoted with permission from Zhu *et al.* Copyright (2022) Elsevier[119].

The fabrication of MXene composites with metal sulfides is a common strategy for exploring new materials. A petal-like $MoS_2/Ti_3C_2T_x$ composite was prepared using a hydrothermal method[108]. MXene acts as a substrate to improve the conductivity of the composite, and MoS_2 grows on the MXene surface to provide abundant active sites for Mg^{2+} storage. The TEM images show that $MoS_2/Ti_3C_2T_x$ has a fluffy petal-like nanosheet morphology and that the MoS_2 layers in the composite are thinner than those in bare MoS_2, which is beneficial for exposing more active sites and Mg-ion diffusion channels. Owing to the high conductivity and abundant surface functional groups of MXene, coupled with the high capacity of few-layer MoS_2 nanosheets, $MoS_2/Ti_3C_2T_x$ exhibits excellent electrochemical capacity (165 mA h g^{-1} at 0.05 A g^{-1}) [Figure 14C]. In addition to MoS_2, CuS has been shown to combine with MXene via a hydrothermal method[118]. CuS nanocrystals are vertically distributed on delaminated $Ti_3C_2T_x$ [Figure 14D]. The S 2p spectrum shows the two peaks at 163.66 and 164.72 eV assigned to the S-Ti-C bond, which demonstrates that CuS is anchored on the MXene surface through S-Ti-C interfacial covalent bonds, resulting in the formation of a CuS/d-$Ti_3C_2T_x$ heterostructure. The strong coupling between CuS and d-$Ti_3C_2T_x$ can contribute to maintaining structural stability and providing a fast charge transfer channel. DFT calculations confirmed that CuS/d-$Ti_3C_2T_x$ exhibits a higher density of states and stronger Mg adsorption than CuS, which facilitates charge transfer and promotes reaction kinetics. The CuS/d-$Ti_3C_2T_x$ heterostructure exhibits a capacity of 336.5 mA h g^{-1} at 0.05 A g^{-1} and still has a capacity of 92.2 mA h g^{-1} upon 1,000 cycles at 1 A g^{-1}.

Therefore, a few-layer metal sulfide can be combined with MXenes to achieve higher capacity and stronger stability.

In addition, V-based sulfides can be combined with MXenes via hydrothermal and electrostatic self-assembly strategies. VS_4 nanosheets have been generated *in situ* on a carbon-coated Ti_3C_2 MXene matrix (denoted as VS_4@Ti_3C_2/C)[119]. According to the V 2p spectrum, two peaks were observed at 513.8 and 521.3 eV, with respect to the V-C bond. This indicates that VS_4 is anchored to the surface of Ti_3C_2. As shown in the SEM images in Figure 14E-G, owing to the MXene and VS_4 composite structural design, the morphology of VS_4 changed from a dense microsphere to a nanosheet structure; thus, VS_4 could expose more active sites and increase the contact area with the electrolyte. VS_4@Ti_3C_2/C with a unique 2D hierarchical nano-micro structure exhibited a capacity of 492 mA h g^{-1} at 50 mA g^{-1} and could be cycled over 900 cycles. The electrolyte in the battery was 0.25 M methylpyrrolidinium chloride + 0.25 M 2PhMgCl-$AlCl_3$ /tetrahydrofuran. *Ex-situ* XRD and XPS analyses revealed the reversible insertion/extraction mechanism of $MgCl^+$. Compared to Mg^{2+}, $MgCl^+$ exhibited a lower migration energy barrier in the cathode structure, leading to a superior electrochemical performance. In summary, when MXenes are combined with sulfides, the key to enhancing the composite capacity is to increase the number of active sites. The large specific surface area of MXenes allows sulfides to expose more active sites in the composites. The electrochemical properties of MXene/sulfur-based material composites as cathodes are summarized in Table 3[108,109,112,116-119].

MXene/selenium-based material composites as cathodes

Selenium-based material as cathodes

Selenium is less electronegative than oxygen and sulfur, facilitating the reduction of strong interactions between the host material and the intercalated ions. Therefore, selenium-based materials have a broad range of applications in MMIBs. Classical layered selenides have also received considerable attention. Their metal atoms covalently bond with adjacent selenium layers to form an interlayer structure (Se-M-Se), and the individual interlayer structures of Se-M-Se are connected via van der Waals forces. These properties allow rapid ion transport in the channels[120]. However, the electrochemical stability of metal selenides is poor, mainly owing to their low electrical conductivity, volume expansion, and dissolution of the cathode active material during cycling. In addition, stacking problems may occur in layered selenides. Pure VSe_2 exhibits a discharge capacity of 159.6 mA h g^{-1} at 0.5 A g^{-1} in ZIBs[121]. Therefore, the combination of selenium-based materials with MXenes having high conductivity and large ion channels can inhibit the lattice distortion caused by anion insertion during cycling and contribute to the stability of the electrode structure.

MXene/selenium-based material composites as cathodes in AIBs

MXene/selenium-based material composites provide the possibility of advanced cathodes for AIBs. The 2D composite was prepared by mixing V_2C powder with selenium (V_2C@Se) at a mass ratio of 1:2 and calcining it at a temperature of 500 °C [Figure 15A][122]. After selenium doping, large amounts of V^{2+} were oxidized to V^{4+}, and functional groups such as -O, -OH, -F and -Cl on the surface of V_2C were reduced and replaced by selenium atoms[123]. Selenium is also involved in redox reactions, and reversible transformation of Se^{2-} and Se^{2+} occurs during charging and discharging [Figure 15B]. Therefore, the reversible redox reactions on the V_2C@Se cathode are mainly V^{2+}/V^{3+}, V^{4+}/V^{5+}, and Se^{2-}/Se^{2+}. The capacity of the V_2C@Se reached 402.5 mA h g^{-1} at 1 A g^{-1}, and after 1,000 cycles, the capacity still reaches 119.8 mA h g^{-1}.

To explore the mechanism of poor cycling stability and low Coulombic efficiency in AIBs, Yuan *et al.* analyzed the effect of embedding common carriers ($AlCl^-_4$, $Al_2Cl^-_7$, Al^{3+}, and Cl^-) in $CoSe_2$ lattices via DFT[124]. As shown in Figure 15C, the insertion of $AlCl^-_4$ into the $CoSe_2$ material required a large amount of energy (3.30 eV). In contrast, the energies required for the insertion of Al^{3+} and Cl^- into the $CoSe_2$ material

Table 3. Summary of the electrochemical properties of MXene/sulfur-based material composites as cathodes

Battery system	Cathode materials	Capacity	Cycle stability	Ref.
ZIBs	$VS_2 \perp V_4C_3T_x$	273.9 mA h g^{-1} at 1 A g^{-1}	69.6% after 2,000 cycles at 5 A g^{-1}	[109]
AIBs	Co_9S_8NP@NPC@MXene	277 mA h g^{-1} at 0.1 A g^{-1}	66.1% after 1,000 cycles at 1 A g^{-1}	[112]
	$CoSe_2$@NPC@MXene	288 mA h g^{-1} at 1 A g^{-1}	76.4% after 300 cycles at 1 A g^{-1}	[112]
MIBs	S_8-CNT-MXene	530 mA h g^{-1} at 0.05 A g^{-1}	83% after 25 cycles at 0.05 A g^{-1}	[116]
	Ti_3C_2@CoO	1,540 mA h g^{-1} at 0.1 A g^{-1}	35.1% after 70 cycles at 0.1 A g^{-1}	[117]
	$MoS_2/Ti_3C_2T_x$	165 mA h g^{-1} at 0.05 A g^{-1}	65.5% after 50 cycles at 0.05 A g^{-1}	[108]
	CuS/d-$Ti_3C_2T_x$	336.5 mA h g^{-1} at 0.05 A g^{-1}	75% after 1,000 cycles at 1 A g^{-1}	[118]
	$VS_4@Ti_3C_2$/C	492 mA h g^{-1} at 0.05 A g^{-1}	80% after 900 cycles at 0.5 A g^{-1}	[119]

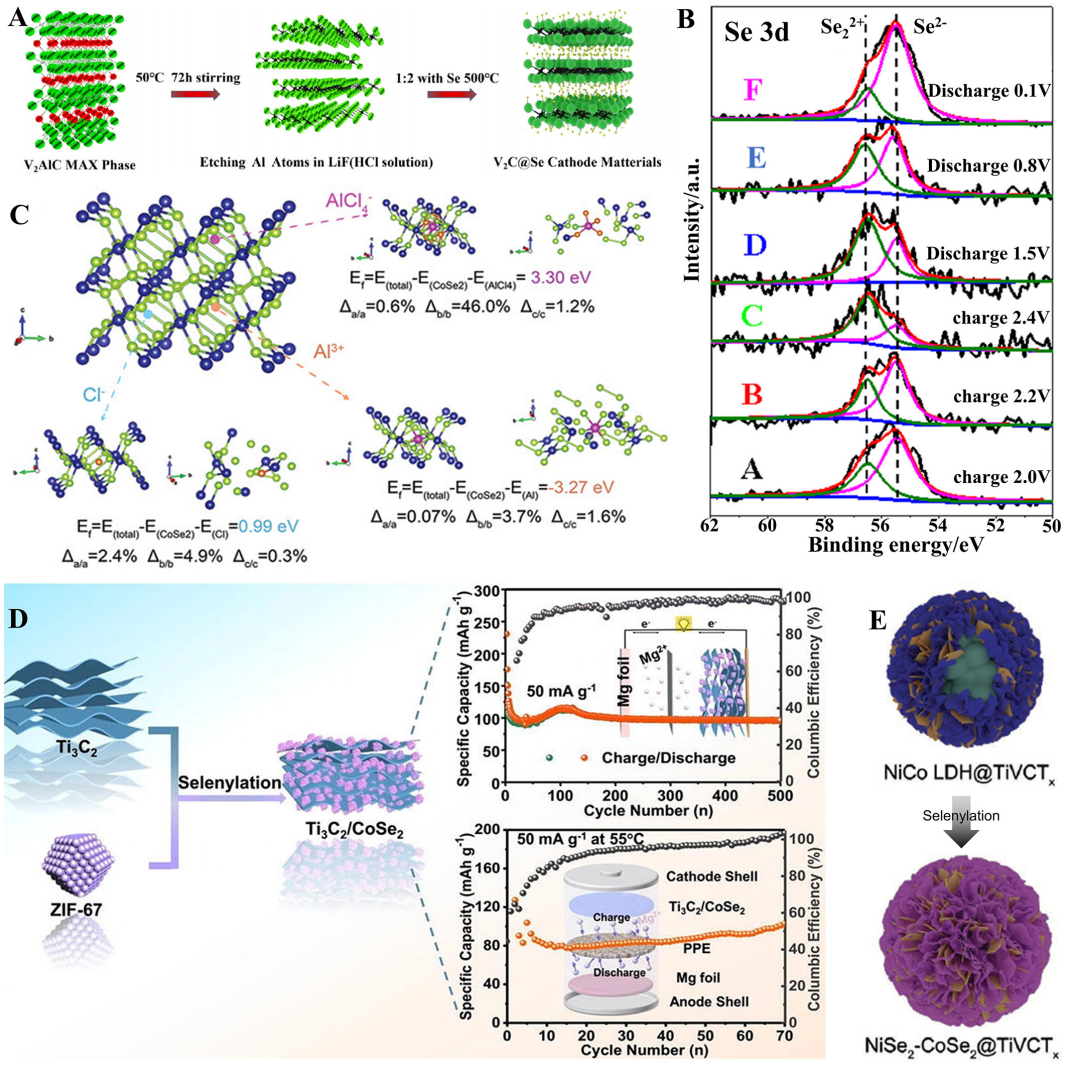

Figure 15. (A) Schematic of the preparation process of V_2C@Se. (B) XPS spectra of Se 3d in V_2C@Se during charging and discharging process. This figure is quoted with permission from Lv *et al.* Copyright (2022) Elsevier[122]. (C) Theoretical simulation analysis with $AlCl^-_4$, Cl^-, and Al^{3+} entering $CoSe_2$. This figure is quoted with permission from Yuan *et al.* Copyright (2023) John Wiley and Sons[124]. (D) Schematic illustration of the $Ti_3C_2/CoSe_2$ synthesis and electrochemical performance. This figure is quoted with permission from Liu *et al.* Copyright (2021) Elsevier[125]. (E) Schematic illustration of the NCSe@TiVC heterostructure. This figure is quoted with permission from Zhang *et al.* Copyright (2022) John Wiley and Sons[126].

were -3.27 and 0.99 eV, respectively, which did not cause large lattice distortions. Therefore, the growth of $CoSe_2$ on the surface of MXene can enhance the performance of cathode materials by suppressing lattice distortion. The $CoSe_2$@TiO_2/Ti_3C_2 cathode provided a stable discharge capacity of 197 mA h g^{-1} at 0.2 A g^{-1}, and a retaining capacity of 102 mA h g^{-1} after 500 cycles at 1.6 A g^{-1} (the capacity of $CoSe_2$ cathode was only 25 mA h g^{-1}).

MXene/selenium-based material composites as cathodes in MIBs

Utilizing metal-organic frames (MOFs) to induce metal selenides is an effective strategy for preparing cathode materials. The Ti_3C_2/$CoSe_2$ heterostructure was prepared by the *in-situ* selenization of the Ti_3C_2/ZIF-67 composite [Figure 15D][125]. The O 1s spectrum revealed a peak at 529.1 eV, which was assigned to Co-O-Ti, suggesting a strong covalent bond between the Co atoms in $CoSe_2$ and the oxygen-containing functional groups from Ti_3C_2. In the heterostructure Ti_3C_2/$CoSe_2$, $CoSe_2$ provides a high capacity for Mg-ion storage, and MXene acts as a structural skeleton and promotes rapid charge transfer at the interface. Therefore, electrodes exhibit an excellent rate performance (75.7 mA h g^{-1} at 1,000 m A g^{-1}) and cycling stability (79% capacity retention after 500 cycles). Significantly, Ti_3C_2/$CoSe_2$ matched with gel polymer electrolytes exhibits outstanding electrochemical performance (67.3 mA h g^{-1} at 50 mA g^{-1} over 70 cycles) in quasi-solid-state MIBs.

MOFs, as self-sacrificing templates, were reported to combine with $TiVCT_x$ MXene, resulting in the formation of a $NiSe_2$-$CoSe_2$@$TiVCT_x$ (NCSe@TiVC) heterostructure [Figure 15E][126]. The SEM images showed a unique 3D porous spherical structure with many active sites. DFT calculations and electrochemical impedance spectroscopy (EIS) proved that the conductivity of NCSe@TiVC was significantly improved compared with that of $NiSe_2$-$CoSe_2$. In addition, DFT was used to analyze the optimal Mg-ion adsorption sites in the structure and demonstrate that the as-prepared heterostructure promoted rapid charge transfer. NCSe@TiVC exhibited excellent electrochemical properties (136 mA h g^{-1} at 0.05 A g^{-1} after 100 cycles). It is worth noting that the assembled flexible pouch-cell device demonstrated excellent electrical performance (104 mA h g^{-1} at 0.1 A g^{-1} upon 200 cycles) when subjected to bending at various angles. The electrochemical properties of MXene/selenium-based material composites as cathodes are summarized in Table 4[122,124-126].

Other MXene composites as cathodes

In addition to the aforementioned materials, combinations of MXenes with other materials possessing numerous ion diffusion pathways and stable structures have also been explored for MMIB cathodes. Specifically, 2D layered double hydroxides (LDHs), iodine (I_2), organic cathodes, and MOFs have been demonstrated to enhance the electrochemical performance of cathodes when combined with MXenes.

Other MXene composites as cathodes in ZIBs

LDHs are special layered materials consisting of multiple positively charged layers with anions in the middle, which can also be used as cathodes for ZIBs. Combining LDHs with MXene can help avoid a sharp drop in the capacity of the LDH cathode during charging and discharging. The 2D/2D Co-doped Ni-Mn-LDH/V_2CT_x MXene (CNMV) was prepared from positively charged Co-doped LDH and negatively charged 2D V_2CT_x MXene using simultaneous ion doping and electrostatic assembly methods[127]. The LDH nanoflowers in the CNMV composite were tightly wrapped around the delaminated MXene nanosheets [Figure 16A]. Benefiting from the Co-ion doping, the layer spacing of the CNMV increased, and the CNMV cathode provided more ion transport channels and reaction sites. When the high conductivity of the 2D V_2CT_x MXene framework was combined with the high electrochemical activity of the Co-doped LDH, the energy density reached 368.7 W h kg^{-1}.

Table 4. Summary of the electrochemical properties of MXene/selenium-based material composites as cathodes

Battery system	Cathode materials	Capacity	Cycle stability	Ref.
AIBs	V_2C@Se	402.5 mA h g^{-1} at 1 A g^{-1}	29.8% after 1,000 cycles at 1 A g^{-1}	[122]
	$CoSe_2$@TiO_2/Ti_3C_2	197 mA h g^{-1} at 0.2 A g^{-1}	88% after 500 cycles at 1.6 A g^{-1}	[124]
MIBs	Ti_3C_2/$CoSe_2$	75.7 mA h g^{-1} at 1 A g^{-1}	79% after 500 cycles at 0.05 A g^{-1}	[125]
	NCSe@TiVC	136 mA h g^{-1} at 0.05 A g^{-1}	93.6% after 500 cycles at 0.5 A g^{-1}	[126]

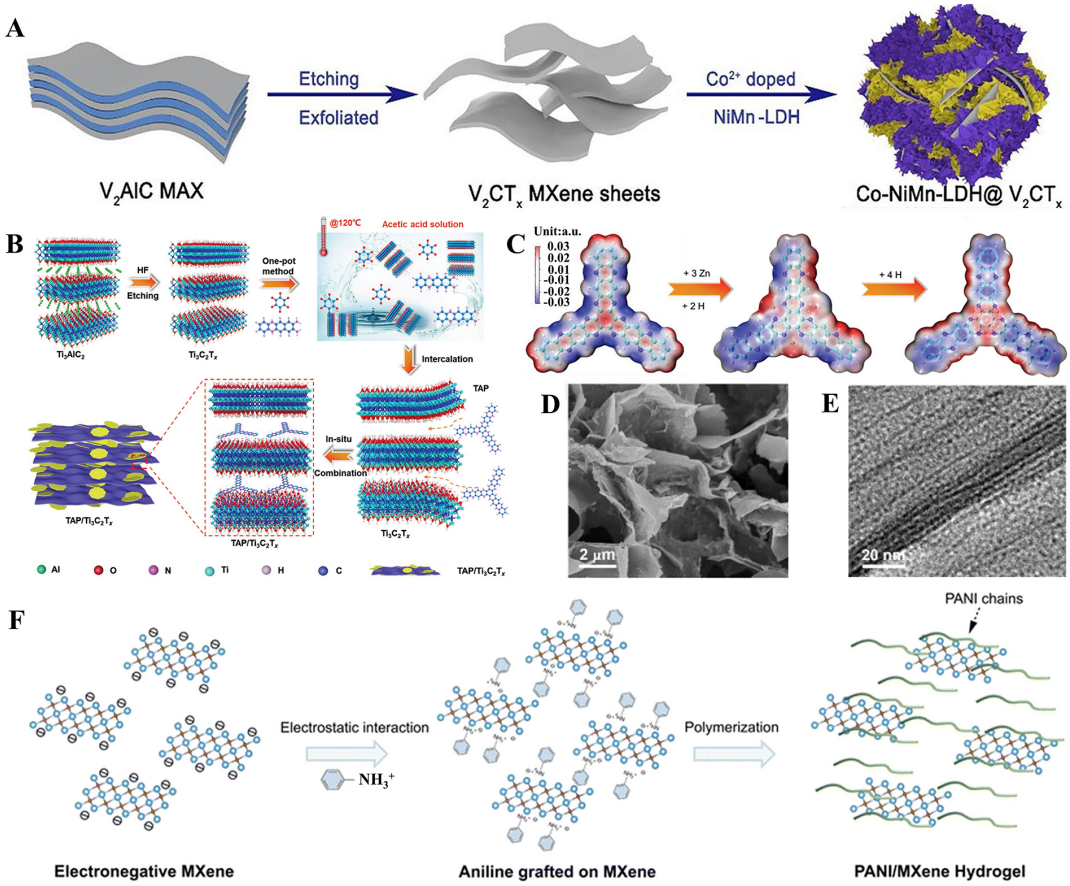

Figure 16. (A) Schematic representation for the synthesis of CNMV hybrid. This figure is quoted with permission from Zhang *et al.* Copyright (2021) Elsevier[127]. (B) Schematic illustration for the synthesis method of TAP/$Ti_3C_2T_x$. (C) Electrostatic potential of TAP molecule after storing Zn^{2+} and H^+ ions. This figure is quoted with permission from Wang *et al.* Copyright (2022) John Wiley and Sons[130]. (D) SEM image of Cu-HHTP/MXene. (E) HRTEM image of Cu-HHTP/MXene. This figure is quoted with permission from Wang *et al.* Copyright (2022) John Wiley and Sons[31]. (F) Schematic illustration for preparation of polyaniline/MXene hydrogel by chemical oxidation polymerization. This figure is quoted with permission from Wang *et al.* Copyright (2024) Royal Society of Chemistry[134].

I_2-Zn batteries have been studied extensively owing to their low cost and safety[128]. However, because elemental I_2 is insulating, excellent substrate conductivity is required to ensure fast electron transport. In addition, the shuttle effect of the I species (I_2, I^-, and I^-_3) during cycling causes a loss of active material, leading to capacity decay. The emergence of MXenes has provided a new approach to realize high-performance I_2-Zn batteries. The electrodeposited I_2-Nb_2CT_x MXene material (eIM) was prepared by inserting I^- ions into the MXene layers under an electric field and *in-situ* oxidization of I^- into linear I_2 molecules at 1.6 V[129]. In the eIM, linear I_2 molecules were uniformly distributed on the highly conductive Nb_2CT_x MXene surface, providing more active sites and enabling fast electron transport. However, the

nanoscale interlayer spacing of Nb_2CT_x MXene restricted the I species to the interlayer, reducing the loss of the active material. Therefore, the I_2-Zn battery with eIM as the cathode has an excellent rate performance (205 mA h g^{-1} at 1.0 A g^{-1} and 143 mA h g^{-1} at 18 A g^{-1}).

In addition to various inorganic materials, MXenes can be combined with organic cathodes to improve the electrochemical performance. Tri (aza) pentaenene (TAP), which has extended conjugated effects along the C=N chains, was injected into $Ti_3C_2T_X$ MXene, and the obtained TAP/$Ti_3C_2T_X$ composite is shown in Figure 16B[130]. Because of steric effects, the abundant C=N sites in the TAP molecules can selectively store H^+ and Zn^{2+}. Based on the electrostatic potential of the TAP molecule [Figure 16C], the C=N bonds with the lowest electrostatic potential in the blue region can store H^+ and Zn^{2+} ions[131,132]. The calculation results based on the charge density difference and Bader charge showed charge depletion on the surface of $Ti_3C_2T_x$ and charge accumulation on the surface of the TAP. This demonstrated the intimate electronic interactions between TAP and $Ti_3C_2T_x$, which maintained the structural stability of the TAP/$Ti_3C_2T_x$ cathode. The TAP/$Ti_3C_2T_x$ cathode exhibited a discharge capacity of 303 mA h g^{-1} at 0.04 A g^{-1} and remarkable cycle stability of 10,000 times at 1 A g^{-1}.

MOFs are also used as advanced energy-storage materials owing to their large one-dimensional channel in MOFs[133]. The combination with MXenes is expected to enhance the electrical conductivity and structural stability. The Cu-HHTP/MXene heterostructure material consists of alternating stacks of Cu-HHTP MOF and MXene formed by electrostatic self-assembly[31]. The SEM [Figure 16D] and HRTEM images [Figure 16E] of Cu-HHTP/MXene showed a multilayer nanosheet stack structure. Cu-HHTP and MXene have an excellent synergistic effect; MXene nanosheets, as structural frameworks, can improve the electrical conductivity and prevent Cu-HHTP aggregation during cycling. Accordingly, the Cu-HHTP layers contribute to the capacity and act as spacer layers for the MXene nanosheets, preventing these nanosheets from stacking. The Cu-HHTP/MXene cathode has achieved a significant capacity of 260.1 mA h g^{-1} at 0.1 A g^{-1} and a long cycle stability over 1,000 cycles with 92.5% capacity retention at 4 A g^{-1}. Instead of using electrostatic adsorption to prepare heterostructures, organic molecules can be linked to MXenes through chemical reactions to form bonds. Polyaniline (PANI)/MXene hydrogels were synthesized via the rapid chemical oxidative polymerization of MXene and aniline monomers[134]. The MXene nanosheets in the hybrid hydrogel interacted with the PANI chain through hydrogen bonding to form a 3D network structure, thereby significantly enhancing the electrochemical reactivity and stability [Figure 16F]. In addition, the 3D PANI/MXene network structure allowed rapid ion and electron transport and enhanced the reaction kinetics.

Other MXene composites as cathodes in AIBs

Organic cathodes are also an important research topic for AIBs. Although most organic cathodes are environmentally friendly and have a long cycle life, they have a low specific capacity. Combining organic cathodes with MXenes is expected to increase battery capacity. The anthraquinone derivative benzo[1,2-b:4,5-b′]dithiophene-4,8-dione (BDTO) and Ti_3C_2 MXene composite (MXene@BDTO) was synthesized using a hydrothermal method [Figure 17A][135]. Based on the SEM images of the MXene@BDTO and BDTO powders, BDTO was attached to the MXene layers in MXene@BDTO [Figure 17B], whereas the BDTO powders were stacked together [Figure 17C]. The MXene@BDTO structure inhibited the dissolution of BDTO and provided active reaction sites[136]. In addition, certain Ti metal ions in MXene reacted with the C=O bonds in BDTO, resulting in the formation of C-O-Ti bonds, which enhanced the stability of structure. Therefore, the MXene@BDTO cathode exhibited an initial capacity of 229.8 mA h g^{-1} at 0.5 A g^{-1} and retained a discharge capacity of 134.9 mA h g^{-1} even after 500 cycles. The electrochemical properties of other MXene composites as cathodes are summarized in Table 5[31,127,129,130,134,135].

Table 5. Summary of the electrochemical properties of other MXene composites as cathodes

Battery system	Cathode materials	Capacity	Cycle stability	Ref.
ZIBs	CNMV	322.7 mA h g^{-1} at 0.2 A g^{-1}	95.7% after 600 cycles at 1 A g^{-1}	[127]
	I_2-Nb_2CT_x	205 mA h g^{-1} at 1 A g^{-1}	80% after 23,000 cycles at 6 A g^{-1}	[129]
	TAP/$Ti_3C_2T_x$	303 mA h g^{-1} at 0.04 A g^{-1}	81.6% after 10,000 cycles at 1 A g^{-1}	[130]
	Cu-HHTP/MXene	260.1 mA h g^{-1} at 0.1 A g^{-1}	92.5% after 1,000 cycles at 4 A g^{-1}	[31]
	PANI/MXene	219 mA h g^{-1} at 0.2 A g^{-1}	88.3% after 5,000 cycles at 5 A g^{-1}	[134]
AIBs	MXene@BDTO	229.8 mA h g^{-1} at 0.5 A g^{-1}	58.7% after 500 cycles at 0.5 A g^{-1}	[135]

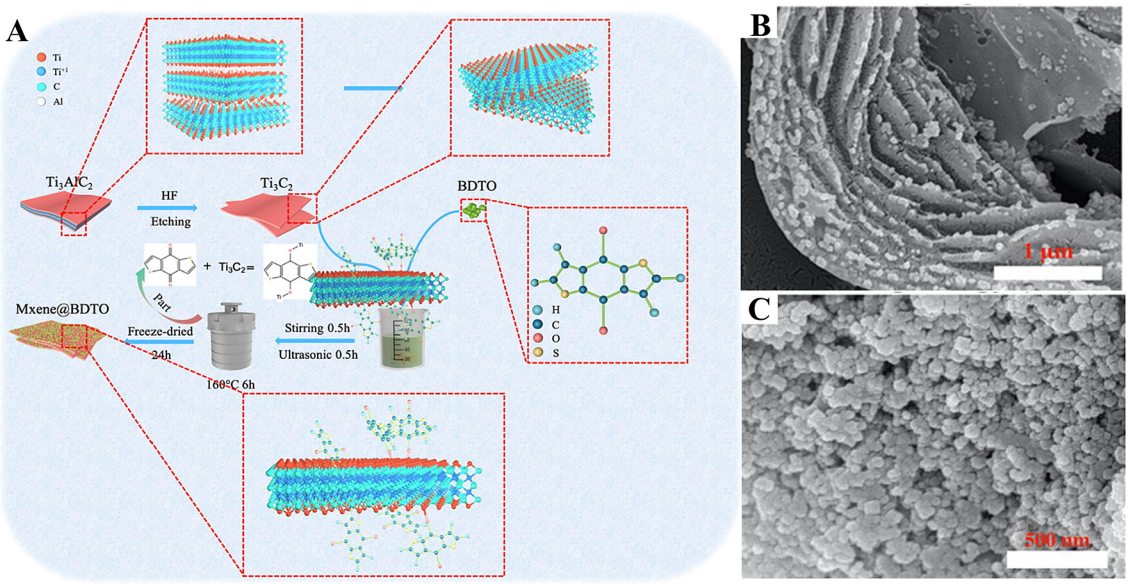

Figure 17. (A) Schematic representation of the synthetic process of MXene@BDTO. (B) SEM image of MXene@BDTO. (C) SEM image of BDTO powders. This figure is quoted with permission from Wu *et al.* Copyright (2022) Elsevier[135].

CONCLUSIONS AND PERSPECTIVES

This review summarizes the progress of MXenes as cathodes for MMIBs. In MMIBs, cathode materials, as host materials for metal ion intercalation/deintercalation, encounter the following main challenge: The high charge density carried by multivalent metal ions can generate strong Coulombic interactions with the cathode material, leading to high energy barriers, which may induce adverse changes, such as irreversible phase transition, dissolution of active materials, and structural collapse of the cathode material. Therefore, it is crucial to improve the conductivity of charge carriers and expand the ion accommodation space to enhance cathode performance. MXenes, as 2D layered transition metal carbon/nitrides, have outstanding electrical conductivity that promotes charge transfer and accelerates electrochemical reaction kinetics. Moreover, their high surface area is conducive to increasing the number of active sites, which can accommodate more ions. In addition, MXenes exhibit other physicochemical properties, including superior mechanical properties, excellent chemical stability, and strong adjustability. Therefore, MXenes can serve not only as host materials for energy storage, but also as matrices that can be combined with other materials to enhance the electrical conductivity and increase the number of active sites of the cathode, thereby enhancing the electrochemical performance.

When MXenes are employed as the cathode material in MMIBs, the strong correlation between the properties of the charge carriers and the electrochemical properties of MXenes is a crucial aspect that must

be considered. During the cycling process, the metal ions in the electrolyte enter the lattice interstices of MXenes. First, the metal ions must undergo desolvation at the electrolyte-electrode interface before intercalation. However, because of the high charge of multivalent ions, there is a strong interaction between multivalent ions and solvent molecules such as $Zn(H_2O)_x^{2+}$, $MgCl^+$, and $AlCl^-_4$, leading to slow ion diffusion, high interface transfer resistance, and low stability of the cathode structure. When metal ions enter the layered MXenes from the interface, owing to the difference in site energy and coordination preferences of multivalent metal ions in the cathode structure, the metal ions exhibit different migration energy barriers. In a layered MXene structure, Zn^{2+} has a common coordination number (4), whereas Mg^{2+} and Al^{3+} have a coordination number of 6. Therefore, the migration energy barrier of Zn ions is lower than that of Mg ions, whereas Al ions exhibit a high migration energy barrier owing to the strong electrostatic interactions caused by their high charge density. In addition, the electrostatic interactions between multivalent metal ions and MXenes are different, leading to ion hysteresis in the cathode, which triggers structural collapse and irreversible phase transitions, significantly affecting the battery cycle life.

Although significant progress has been made in the application of MXenes as cathodes, there is still room for further development. Therefore, based on our understanding of how to promote the advancement of MXenes, we propose several suggestions and directions.

1. The MXene cathodes in MMIBs are predominantly Ti_3C_2 and V_2C. Consequently, it is necessary to explore other MXenes for potential application in MMIBs. Moreover, MXenes have many different terminal groups, such as F, S, Te, Se, and NH. Their terminal functional groups can be customized to meet specific performance requirements. However, the impact of terminal groups on performance has rarely been investigated. Therefore, the roles of different terminal groups on the cathodes of MMIBs should be explored, and more attention should be paid to other MXene composites. In the future, the combination of MXenes and other active materials, which may create unexpected effects, should be investigated further.

2. When MXenes or their composites are used as cathode materials, their stabilities must be considered. Owing to the strong hydrogen bonds and interlayer van der Waals forces of MXenes, they tend to agglomerate and stack during cycling, leading to a reduction in the number of active sites and an acceleration of the structural collapse of the composite. Moreover, MXenes are sensitive to water and oxygen and their surfaces are easily oxidized. Therefore, to ensure the stability of the cathode structure, it is necessary to focus on improving the stability of MXenes.

3. MXene application scenarios should be expanded, and additional MXene properties and functions should be explored. MXenes have great application potential, but research on their electrochemical performance over a wide range of temperatures is insufficient. In the future, additional applications of MXenes in high- and low-temperature environments should be explored. Moreover, the significant flexibility of MXenes is an outstanding advantage for flexible batteries. Thus, the design of flexible MXene composites could be improved by including more application scenarios in the future. In addition, areas such as microbatteries and degradable batteries will become future research hotspots, and the application of MXenes in these areas should also be considered.

4. Currently, most synthetic solutions for MXenes are based on HF or fluorine-based salt etching. These etchers cause environmental pollution and operational risks, which hinder the large-scale production of MXenes. In addition, fluorine-based etchers inevitably introduce the F element, which is harmful to green manufacturing and limits the application of MXenes. As research and synthesis technologies continue to advance, novel synthesis approaches, such as CVD, are being explored, and MXenes will have broader

application prospects in the field of MMIBs. Notably, 3D MXenes are conducive for increasing the number of active sites of the material. Combining 3D MXenes with other materials can alleviate the volume expansion problem of cathode materials. Therefore, more attention should be paid to the applications of 3D MXenes in future studies.

5. There are still many urgent problems that need to be solved for cathode materials in MMIBs. The electrochemical stability and capacity of multivalent ion batteries require further enhancement. This is the key to reducing the migration barrier of multicharged ions in MXenes. Defect engineering has been proven to be an effective strategy. Nevertheless, the loss of lattice oxygen and transformation of local structures can potentially lead to structural collapse. It is worth exploring future directions for accurately regulating the local structure to improve the material properties. The high charge density of multivalent metal ions results in high solvation energy. Employing MXenes with tunable functional group properties to achieve the rapid desolvation of metal ions at interfaces represents a promising direction. In addition, the energy-storage mechanism of cathode materials must be further explored.

6. The batteries studied mainly involved coin-type cells, which tend to be proof-of-concept and cannot accurately evaluate the effects of MXenes in practical applications. Therefore, future studies should examine other battery types, including pouch and cylindrical batteries. In addition, to achieve large-scale applications, researchers should focus on the electrochemical performance of batteries at low current densities and cathode materials with high loads and consider practical issues such as cost, safety, and environmental protection[98].

In summary, MXenes have broad application prospects as advanced cathodes in MMIBs. We hope that this review will help readers better understand the applications of MXenes as cathodes in MMIBs. We also hope that MXenes will overcome these challenges as soon as possible and achieve large-scale commercial applications.

DECLARATIONS

Authors' contributions

Manuscript drafting and editing and technical support: Zhao X, Ruan C
Substantial contributions to conception and design of the study, and manuscript editing: Wang S, Liu H
Assistance in the design of the study, and administrative support: Sang Y

Availability of data and materials

Not applicable.

Financial support and sponsorship

This work is supported by the National Natural Science Foundation of China (Grant no. 92372118, 52072224).

Conflicts of interest

All authors declared that there are no conflicts of interest.

Ethical approval and consent to participate

Not applicable.

Consent for publication

Not applicable.

REFERENCES

1. Zhang N, Chen X, Yu M, Niu Z, Cheng F, Chen J. Materials chemistry for rechargeable zinc-ion batteries. *Chem Soc Rev* 2020;49:4203-19. DOI
2. Chao D, Zhou W, Xie F, et al. Roadmap for advanced aqueous batteries: from design of materials to applications. *Sci Adv* 2020;6:eaba4098. DOI PubMed PMC
3. Yao H, Yu H, Zheng Y, et al. Pre-intercalation of ammonium ions in layered δ-MnO_2 nanosheets for high-performance aqueous zinc-ion batteries. *Angew Chem Int Ed* 2023;62:e202315257. DOI
4. Zhao Y, Zhang S, Zhang Y, et al. Vacancy-rich Al-doped MnO_2 cathodes break the trade-off between kinetics and stability for high-performance aqueous Zn-ion batteries. *Energy Environ Sci* 2024;17:1279-90. DOI
5. Zhong C, Liu B, Ding J, et al. Decoupling electrolytes towards stable and high-energy rechargeable aqueous zinc-manganese dioxide batteries. *Nat Energy* 2020;5:440-9. DOI
6. Li H, Zhang F, Wei W, et al. Promoting air stability of Li anode via an artificial organic/inorganic hybrid layer for dendrite-free lithium batteries. *Adv Energy Mater* 2023;13:2301023. DOI
7. Wu F, Maier J, Yu Y. Guidelines and trends for next-generation rechargeable lithium and lithium-ion batteries. *Chem Soc Rev* 2020;49:1569-614. DOI PubMed
8. Jing F, Liu Y, Shang Y, et al. Dual ions intercalation drives high-performance aqueous Zn-ion storage on birnessite-type manganese oxides cathode. *Energy Stor Mater* 2022;49:164-71. DOI
9. Yang X, Wang X, Xiang Y, Ma L, Huang W. Asymmetric electrolytes design for aqueous multivalent metal ion batteries. *Nanomicro Lett* 2023;16:51. DOI PubMed PMC
10. Chen S, Zhao D, Chen L, et al. Emerging intercalation cathode materials for multivalent metal-ion batteries: status and challenges. *Small Struct* 2021;2:2100082. DOI
11. Pan Z, Liu X, Yang J, et al. Aqueous rechargeable multivalent metal-ion batteries: advances and challenges. *Adv Energy Mater* 2021;11:2100608. DOI
12. Liang Y, Dong H, Aurbach D, Yao Y. Current status and future directions of multivalent metal-ion batteries. *Nat Energy* 2020;5:646-56. DOI
13. Liu Z, Qin L, Cao X, et al. Ion migration and defect effect of electrode materials in multivalent-ion batteries. *Prog Mater Sci* 2022;125:100911. DOI
14. Zhang CJ, Anasori B, Seral-Ascaso A, et al. Transparent, flexible, and conductive 2D titanium carbide (MXene) films with high volumetric capacitance. *Adv Mater* 2017;29:1702678. DOI
15. Amiri A, Chen Y, Bee Teng C, Naraghi M. Porous nitrogen-doped MXene-based electrodes for capacitive deionization. *Energy Stor Mater* 2020;25:731-9. DOI
16. Ling Z, Ren CE, Zhao MQ, et al. Flexible and conductive MXene films and nanocomposites with high capacitance. *Proc Natl Acad Sci USA* 2014;111:16676-81. DOI PubMed PMC
17. An Y, Tian Y, Shen H, Man Q, Xiong S, Feng J. Two-dimensional MXenes for flexible energy storage devices. *Energy Environ Sci* 2023;16:4191-250. DOI
18. Abid MZ, Rafiq K, Aslam A, Jin R, Hussain E. Scope, evaluation and current perspectives of MXene synthesis strategies for state of the art applications. *J Mater Chem A* 2024;12:7351-95. DOI
19. Jing H, Yeo H, Lyu B, et al. Modulation of the electronic properties of MXene ($Ti_3C_2T_x$) via surface-covalent functionalization with diazonium. *ACS Nano* 2021;15:1388-96. DOI
20. Tian Y, An Y, Feng J, Qian Y. MXenes and their derivatives for advanced aqueous rechargeable batteries. *Mater Today* 2022;52:225-49. DOI
21. Liu H, Ma Y, Cao B, Zhu Q, Xu B. Recent progress of MXenes in aqueous zinc-ion batteries. *Acta Phys Chim Sin* 2023;39:2210027. DOI
22. Liu P, Liu W, Liu K. Rational modulation of emerging MXene materials for zinc-ion storage. *Carbon Energy* 2022;4:60-76. DOI
23. Javed MS, Mateen A, Ali S, et al. The emergence of 2D MXenes based Zn-ion batteries: recent development and prospects. *Small* 2022;18:e2201989. DOI
24. Wei C, Tao Y, An Y, et al. Recent advances of emerging 2D MXene for stable and dendrite-free metal anodes. *Adv Funct Mater* 2020;30:2004613. DOI
25. Zheng S, Zhao W, Chen J, Zhao X, Pan Z, Yang X. 2D materials boost advanced Zn anodes: principles, advances, and challenges. *Nanomicro Lett* 2023;15:46. DOI PubMed PMC
26. Wang C, Pan Z, Chen H, Pu X, Chen Z. MXene-based materials for multivalent metal-ion batteries. *Batteries* 2023;9:174. DOI

27. Liu H, Zhang X, Zhu Y, et al. Electrostatic self-assembly of 0D-2D SnO_2 quantum dots/$Ti_3C_2T_x$ MXene hybrids as anode for lithium-ion batteries. *Nanomicro Lett* 2019;11:65. DOI PubMed PMC
28. Xiong D, Shi Y, Yang HY. Rational design of MXene-based films for energy storage: progress, prospects. *Mater Today* 2021;46:183-211. DOI
29. Bashir T, Zhou S, Yang S, et al. Progress in 3D-MXene electrodes for lithium/sodium/potassium/magnesium/zinc/aluminum-ion batteries. *Electrochem Energy Rev* 2023;6:5. DOI
30. Liu Z, Zhang Y, Zhang HB, et al. Electrically conductive aluminum ion-reinforced MXene films for efficient electromagnetic interference shielding. *J Mater Chem C* 2020;8:1673-8. DOI
31. Wang Y, Song J, Wong WY. Constructing 2D sandwich-like MOF/MXene heterostructures for durable and fast aqueous zinc-ion batteries. *Angew Chem Int Ed* 2023;62:e202218343. DOI
32. Wang C, Chen S, Song L. Tuning 2D MXenes by surface controlling and interlayer engineering: methods, properties, and synchrotron radiation characterizations. *Adv Funct Mater* 2020;30:2000869. DOI
33. Dall'agnese Y, Lukatskaya MR, Cook KM, Taberna P, Gogotsi Y, Simon P. High capacitance of surface-modified 2D titanium carbide in acidic electrolyte. *Electrochem Commun* 2014;48:118-22. DOI
34. Chen C, Wang T, Zhao X, et al. Customizing hydrophilic terminations for V_2CT_x MXene toward superior hybrid-ion storage in aqueous zinc batteries. *Adv Funct Mater* 2024;34:2308508. DOI
35. Naguib M, Kurtoglu M, Presser V, et al. Two-dimensional nanocrystals produced by exfoliation of Ti_3AlC_2. *Adv Mater* 2011;23:4248-53. DOI
36. Pang SY, Wong YT, Yuan S, et al. Universal strategy for HF-free facile and rapid synthesis of two-dimensional MXenes as multifunctional energy materials. *J Am Chem Soc* 2019;141:9610-6. DOI
37. Ghidiu M, Lukatskaya MR, Zhao MQ, Gogotsi Y, Barsoum MW. Conductive two-dimensional titanium carbide 'clay' with high volumetric capacitance. *Nature* 2014;516:78-81. DOI PubMed
38. Wu M, He M, Hu Q, et al. Ti_3C_2 MXene-based sensors with high selectivity for NH_3 detection at room temperature. *ACS Sens* 2019;4:2763-70. DOI
39. Liu F, Zhou A, Chen J, et al. Preparation of Ti_3C_2 and Ti_2C MXenes by fluoride salts etching and methane adsorptive properties. *Appl Surf Sci* 2017;416:781-9. DOI
40. Liu D, Wang L, He Y, et al. Enhanced reversible capacity and cyclic performance of lithium-ion batteries using SnO_2 interpenetrated MXene V_2C architecture as anode materials. *Energy Technol* 2021;9:2000753. DOI
41. Wang X, Garnero C, Rochard G, et al. A new etching environment (FeF_3/HCl) for the synthesis of two-dimensional titanium carbide MXenes: a route towards selective reactivity vs. water. *J Mater Chem A* 2017;5:22012-23. DOI
42. Urbankowski P, Anasori B, Makaryan T, et al. Synthesis of two-dimensional titanium nitride Ti_4N_3 (MXene). *Nanoscale* 2016;8:11385-91. DOI
43. Natu V, Pai R, Sokol M, Carey M, Kalra V, Barsoum MW. 2D $Ti_3C_2T_z$ MXene synthesized by water-free etching of Ti_3AlC_2 in polar organic solvents. *Chem* 2020;6:616-30. DOI
44. Yang S, Zhang P, Wang F, et al. Fluoride-free synthesis of two-dimensional titanium carbide (MXene) using a binary aqueous system. *Angew Chem Int Ed* 2018;57:15491-5. DOI
45. Li T, Yao L, Liu Q, et al. Fluorine-free synthesis of high-purity $Ti_3C_2T_x$ (T=OH, O) via alkali treatment. *Angew Chem Int Ed* 2018;57:6115-9. DOI
46. Li M, Lu J, Luo K, et al. Element replacement approach by reaction with lewis acidic molten salts to synthesize nanolaminated MAX phases and MXenes. *J Am Chem Soc* 2019;141:4730-7. DOI
47. Jawaid A, Hassan A, Neher G, et al. Halogen etch of Ti_3AlC_2 MAX phase for MXene fabrication. *ACS Nano* 2021;15:2771-7. DOI
48. Li J, Wang C, Yu Z, Chen Y, Wei L. MXenes for zinc-based electrochemical energy storage devices. *Small* 2023:e2304543. DOI
49. Geng D, Zhao X, Chen Z, et al. Direct synthesis of large-area 2D Mo_2C on in situ grown graphene. *Adv Mater* 2017;29:1702678. DOI
50. Zhang F, Zhang Z, Wang H, et al. Plasma-enhanced pulsed-laser deposition of single-crystalline Mo_2C ultrathin superconducting films. *Phys Rev Mater* 2017;1:034002. DOI
51. Xiao X, Yu H, Jin H, et al. Salt-templated synthesis of 2D metallic MoN and other nitrides. *ACS Nano* 2017;11:2180-6. DOI
52. Wang Q, Yuan H, Zhang M, et al. A highly conductive and supercapacitive MXene/N-CNT electrode material derived from a MXene-co-melamine precursor. *ACS Appl Electron Mater* 2023;5:2506-17. DOI
53. Xu M, Lei S, Qi J, et al. Opening magnesium storage capability of two-dimensional MXene by intercalation of cationic surfactant. *ACS Nano* 2018;12:3733-40. DOI
54. Miao Z, Zhang F, Zhao H, et al. Tailoring local electrolyte solvation structure via a mesoporous molecular sieve for dendrite-free zinc batteries. *Adv Funct Mater* 2022;32:2111635. DOI
55. Kang Y, Zhang F, Li H, et al. Modulating the electrolyte inner solvation structure via low polarity co-solvent for low-temperature aqueous zinc-ion batteries. *Energy Environ Mater* 2024:e12707. DOI
56. Du M, Zhang F, Zhang X, et al. Calcium ion pinned vanadium oxide cathode for high-capacity and long-life aqueous rechargeable zinc-ion batteries. *Sci China Chem* 2020;63:1767-76. DOI
57. Miao Z, Du M, Li H, et al. Constructing nano-channeled tin layer on metal zinc for high-performance zinc-ion batteries anode. *EcoMat* 2021;3:e12125. DOI

58. Wei W, Zhang F, Li H, et al. Modulating the solvation structure and electrode interface through phosphate additive for highly reversible zinc metal anode. *Chem Eng J* 2024;485:149944. DOI
59. Miao Z, Liu Q, Wei W, et al. Unveiling unique steric effect of threonine additive for highly reversible Zn anode. *Nano Energy* 2022;97:107145. DOI
60. Wang C, Xie H, Chen S, et al. Atomic cobalt covalently engineered interlayers for superior lithium-ion storage. *Adv Mater* 2018;30:e1802525. DOI
61. Li M, Li X, Qin G, et al. Halogenated Ti_3C_2 MXenes with electrochemically active terminals for high-performance zinc ion batteries. *ACS Nano* 2021;15:1077-85. DOI
62. Liu Y, Jiang Y, Hu Z, et al. In-situ electrochemically activated surface vanadium valence in V_2C MXene to achieve high capacity and superior rate performance for Zn-ion batteries. *Adv Funct Mater* 2021;31:2008033. DOI
63. Li X, Li M, Yang Q, et al. In situ electrochemical synthesis of MXenes without acid/alkali usage in/for an aqueous zinc ion battery. *Adv Energy Mater* 2020;10:2001791. DOI
64. Guan J, Shao L, Yu L, et al. Two-dimensional $Mg_{0.2}V_2O_5 \cdot nH_2O$ nanobelts derived from V_4C_3 MXenes for highly stable aqueous zinc ion batteries. *Chem Eng J* 2022;443:136502. DOI
65. Zhu X, Wang W, Cao Z, et al. Zn^{2+}-intercalated $V_2O_5 \cdot nH_2O$ derived from V_2CT_x MXene for hyper-stable zinc-ion storage. *J Mater Chem A* 2021;9:17994-8005. DOI
66. Zhu X, Cao Z, Li X, et al. Ion-intercalation regulation of MXene-derived hydrated vanadates for high-rate and long-life Zn-Ion batteries. *Energy Stor Mater* 2022;45:568-77. DOI
67. Sha D, Lu C, He W, et al. Surface selenization strategy for V_2CT_x MXene toward superior Zn-ion storage. *ACS Nano* 2022;16:2711-20. DOI
68. Elia GA, Marquardt K, Hoeppner K, et al. An overview and future perspectives of aluminum batteries. *Adv Mater* 2016;28:7564-79. DOI
69. Wang Y, Gu H, Lu Y, Zhang W, Li Z. The synergistic effect of Lewis acidic etching V_4C_3(MXene)@$CuSe_2$/$CoSe_2$ as an advanced cathode material for aluminum batteries. *J Mater Sci Technol* 2024;177:205-13. DOI
70. Zhao S, Dall'agnese Y, Chu X, Zhao X, Gogotsi Y, Gao Y. Electrochemical interaction of Sn-containing MAX phase (Nb_2SnC) with Li-ions. *ACS Energy Lett* 2019;4:2452-7. DOI
71. Zhao MQ, Xie X, Ren CE, et al. Hollow MXene spheres and 3D macroporous MXene frameworks for Na-ion storage. *Adv Mater* 2017;29:1702410. DOI
72. Wu Y, Sun Y, Zheng J, Rong J, Li H, Niu L. MXenes: advanced materials in potassium ion batteries. *Chem Eng J* 2021;404:126565. DOI
73. Li J, Zeng F, El-Demellawi JK, et al. Nb_2CT_x MXene cathode for high-capacity rechargeable aluminum batteries with prolonged cycle lifetime. *ACS Appl Mater Interfaces* 2022;14:45254-62. DOI
74. Wang L, Wang J, Ouyang B. Computational investigation of MAX as intercalation host for rechargeable aluminum-ion battery. *Adv Energy Mater* 2023;13:2302584. DOI
75. VahidMohammadi A, Hadjikhani A, Shahbazmohamadi S, Beidaghi M. Two-dimensional vanadium carbide (MXene) as a high-capacity cathode material for rechargeable aluminum batteries. *ACS Nano* 2017;11:11135-44. DOI PubMed
76. Yu X, Wang B, Gong D, Xu Z, Lu B. Graphene nanoribbons on highly porous 3D graphene for high-capacity and ultrastable Al-ion batteries. *Adv Mater* 2017;29:1604118. DOI
77. Shen F, Sun Z, Zhao L, et al. Triggering the phase transition and capacity enhancement of Nb_2O_5 for fast-charging lithium-ion storage. *J Mater Chem A* 2021;9:14534-44. DOI
78. Liu F, Liu Y, Zhao X, Liu X, Fan LZ. Pursuit of a high-capacity and long-life Mg-storage cathode by tailoring sandwich-structured MXene@carbon nanosphere composites. *J Mater Chem A* 2019;7:16712-9. DOI
79. Zhu J, Shi R, Liu Y, et al. 3D interwoven MXene networks fabricated by the assistance of bacterial celluloses as high-performance cathode material for rechargeable magnesium battery. *Appl Surf Sci* 2020;528:146985. DOI
80. Zhang Y, Li D, Li J, et al. Flexible $TiVCT_x$ MXene film for high-performance magnesium-ion storage device. *J Colloid Interface Sci* 2024;657:550-8. DOI
81. Zhao X, Zhang F, Li H, et al. Dynamic heterostructure design of MnO_2 for high-performance aqueous zinc-ion batteries. *Energy Environ Sci* 2024;17:3629-40. DOI
82. Song M, Tan H, Chao D, Fan HJ. Recent advances in Zn-ion batteries. *Adv Funct Mater* 2018;28:1802564. DOI
83. Xie M, Zhang X, Wang R, et al. Mn-O bond engineering mitigating Jahn-Teller effects of manganese oxide for aqueous zinc-ion battery applications. *Chem Eng J* 2024;494:152908. DOI
84. Zhao Y, Zhang P, Liang J, et al. Uncovering sulfur doping effect in MnO_2 nanosheets as an efficient cathode for aqueous zinc ion battery. *Energy Stor Mater* 2022;47:424-33. DOI
85. Zhu X, Cao Z, Wang W, et al. Superior-performance aqueous zinc-ion batteries based on the in situ growth of MnO_2 nanosheets on V_2CT_X MXene. *ACS Nano* 2021;15:2971-83. DOI
86. Peng Q, Guo J, Zhang Q, et al. Unique lead adsorption behavior of activated hydroxyl group in two-dimensional titanium carbide. *J Am Chem Soc* 2014;136:4113-6. DOI
87. Wang Y, Liu L, Wang Y, Qu J, Chen Y, Song J. Atomically coupled 2D MnO_2/MXene superlattices for ultrastable and fast aqueous zinc-ion batteries. *ACS Nano* 2023;17:21761-70. DOI

88. Shi M, Wang B, Chen C, Lang J, Yan C, Yan X. 3D high-density MXene@MnO_2 microflowers for advanced aqueous zinc-ion batteries. *J Mater Chem A* 2020;8:24635-44. DOI
89. Wu L, Mei Y, Liu Y, et al. Interfacial synthesis of strongly-coupled δ-MnO_2/MXene heteronanosheets for stable zinc ion batteries with Zn^{2+}-exclusive storage mechanism. *Chem Eng J* 2023;459:141662. DOI
90. Shi M, Wang B, Shen Y, et al. 3D assembly of MXene-stabilized spinel $ZnMn_2O_4$ for highly durable aqueous zinc-ion batteries. *Chem Eng J* 2020;399:125627. DOI
91. Du M, Miao Z, Li H, Sang Y, Liu H, Wang S. Strategies of structural and defect engineering for high-performance rechargeable aqueous zinc-ion batteries. *J Mater Chem A* 2021;9:19245-81. DOI
92. Zhang F, Sun X, Du M, et al. Weaker interactions in Zn^{2+} and organic ion-pre-intercalated vanadium oxide toward highly reversible zinc-ion batteries. *Energy Environ Mater* 2021;4:620-30. DOI
93. Du M, Liu C, Zhang F, et al. Tunable layered (Na,Mn)$V_8O_{20}\cdot nH_2O$ cathode material for high-performance aqueous zinc ion batteries. *Adv Sci* 2020;7:2000083. DOI
94. Dong W, Du M, Zhang F, et al. In situ electrochemical transformation reaction of ammonium-anchored heptavanadate cathode for long-life aqueous zinc-ion batteries. *ACS Appl Mater Interfaces* 2021;13:5034-43. DOI
95. Zhang X, Xue F, Sun X, et al. High-capacity zinc vanadium oxides with long-term cyclability enabled by in-situ electrochemical oxidation as zinc-ion battery cathode. *Chem Eng J* 2022;445:136714. DOI
96. Du M, Miao Z, Li H, et al. Oxygen-vacancy and phosphate coordination triggered strain engineering of vanadium oxide for high-performance aqueous zinc ion storage. *Nano Energy* 2021;89:106477. DOI
97. Zhang F, Du M, Miao Z, et al. Oxygen vacancies and N-doping in organic-inorganic pre-intercalated vanadium oxide for high-performance aqueous zinc-ion batteries. *InfoMat* 2022;4:e12346. DOI
98. Zhang F, Kang Y, Zhao X, et al. Boosting charge carrier transport by layer-stacked $Mn_xV_2O_6/V_2C$ heterostructures for wide-temperature zinc-ion batteries. *Adv Funct Mater* 2024:2402071. DOI
99. Liu C, Xu W, Mei C, Li MC, Xu X, Wu Q. Highly stable $H_2V_3O_8$/Mxene cathode for Zn-ion batteries with superior rate performance and long lifespan. *Chem Eng J* 2021;405:126737. DOI
100. Liang P, Xu T, Zhu K, et al. Heterogeneous interface-boosted zinc storage of $H_2V_3O_8$ nanowire/$Ti_3C_2T_x$ MXene composite toward high-rate and long cycle lifespan aqueous zinc-ion batteries. *Energy Stor Mater* 2022;50:63-74. DOI
101. Xiao B, Chen J, Hu C, et al. 2D dynamic heterogeneous interface coupling endowing extra Zn^{2+} storage. *Adv Funct Mater* 2023;33:2211679. DOI
102. Liu H, Jiang L, Cao B, et al. Van der Waals interaction-driven self-assembly of V_2O_5 nanoplates and MXene for high-performing zinc-ion batteries by suppressing vanadium dissolution. *ACS Nano* 2022;16:14539-48. DOI
103. Zheng J, Xu T, Xia G, Cui WG, Yang Y, Yu X. Water-stabilized vanadyl phosphate monohydrate ultrathin nanosheets toward high voltage Al-ion batteries. *Small* 2023;19:e2207619. DOI
104. Hu P, Zhu T, Wang X, et al. Highly durable $Na_2V_6O_{16}\cdot 1.63H_2O$ nanowire cathode for aqueous zinc-ion battery. *Nano Lett* 2018;18:1758-63. DOI
105. Geng L, Lv G, Xing X, Guo J. Reversible electrochemical intercalation of aluminum in Mo_6S_8. *Chem Mater* 2015;27:4926-9. DOI
106. Hu Y, Ye D, Luo B, et al. A binder-free and free-standing cobalt sulfide@carbon nanotube cathode material for aluminum-ion batteries. *Adv Mater* 2018;30:1703824. DOI
107. Shuai H, Liu R, Li W, et al. Recent advances of transition metal sulfides/selenides cathodes for aqueous zinc-ion batteries. *Adv Energy Mater* 2023;13:2202992. DOI
108. Xu M, Bai N, Li HX, Hu C, Qi J, Yan XB. Synthesis of MXene-supported layered MoS_2 with enhanced electrochemical performance for Mg batteries. *Chin Chem Lett* 2018;29:1313-6. DOI
109. Mao Y, Bai J, Lin S, et al. Two birds with one stone: V_4C_3 MXene synergistically promoted VS_2 cathode and zinc anode for high-performance aqueous zinc-ion batteries. *Small* 2024;20:e2306615. DOI
110. Zhang Y, Cao Z, Liu S, et al. Charge-enriched strategy based on MXene-based polypyrrole layers toward dendrite-free zinc metal anodes. *Adv Energy Mater* 2022;12:2103979. DOI
111. Tian Y, An Y, Yang Y, Xu B. Robust nitrogen/selenium engineered MXene/ZnSe hierarchical multifunctional interfaces for dendrite-free zinc-metal batteries. *Energy Stor Mater* 2022;49:122-34. DOI
112. Yao L, Ju S, Yu X. Rational surface engineering of MXene@N-doped hollow carbon dual-confined cobalt sulfides/selenides for advanced aluminum batteries. *J Mater Chem A* 2021;9:16878-88. DOI
113. Ohno S, Zeier WG. Toward practical solid-state lithium-sulfur batteries: challenges and perspectives. *ACC Mater Res* 2021;2:869-80. DOI
114. Sun R, Hu J, Shi X, et al. Water-soluble cross-linking functional binder for low-cost and high-performance lithium-sulfur batteries. *Adv Funct Mater* 2021;31:2104858. DOI
115. Xiao Z, Li Z, Meng X, Wang R. MXene-engineered lithium-sulfur batteries. *J Mater Chem A* 2019;7:22730-43. DOI
116. Kaland H, Håskjold Fagerli F, Hadler-Jacobsen J, et al. Performance study of MXene/carbon nanotube composites for current collector- and binder-free Mg-S batteries. *ChemSusChem* 2021;14:1864-73. DOI PubMed PMC
117. Xu H, Zhu D, Zhu W, et al. Rational design of high concentration electrolytes and MXene-based sulfur host materials toward high-performance magnesium sulfur batteries. *Chem Eng J* 2022;428:131031. DOI
118. Cheng Z, Xu Y, Zhang X, et al. An interfacial covalent bonding coupled ultrafine CuS-nanocrystals/MXene heterostructure for

efficient and durable magnesium storage. *J Mater Chem A* 2023;11:12176-84. DOI

119. Zhu J, Zhang X, Gao H, et al. VS_4 anchored on Ti_3C_2 MXene as a high-performance cathode material for magnesium ion battery. *J Power Sources* 2022;518:230731. DOI
120. Xu N, Wu KH, Miao QS, Zhou XM, Sheng LZ. Application of metal selenide anode materials in sodium-ion batteries. *J Changsha Univ Sci Technol* 2024;21:1-11. DOI
121. Narayanasamy M, Hu L, Kirubasankar B, Liu Z, Angaiah S, Yan C. Nanohybrid engineering of the vertically confined marigold structure of rGO-VSe_2 as an advanced cathode material for aqueous zinc-ion battery. *J Alloy Compd* 2021;882:160704. DOI
122. Lv W, Wu G, Li X, Li J, Li Z. Two-dimensional V_2C@Se (MXene) composite cathode material for high-performance rechargeable aluminum batteries. *Energy Stor Mater* 2022;46:138-46. DOI
123. Li Z, Wang X, Zhang W, Yang S. Two-dimensional Ti_3C_2@CTAB-Se (MXene) composite cathode material for high-performance rechargeable aluminum batteries. *Chem Eng J* 2020;398:125679. DOI
124. Yuan Z, Lin Q, Li Y, Han W, Wang L. Effects of multiple ion reactions based on a $CoSe_2$/MXene cathode in aluminum-ion batteries. *Adv Mater* 2023;35:e2211527. DOI
125. Liu F, Wang T, Liu X, Jiang N, Fan LZ. High-performance heterojunction Ti_3C_2/$CoSe_2$ with both intercalation and conversion storage mechanisms for magnesium batteries. *Chem Eng J* 2021;426:130747. DOI
126. Zhang Y, Cao JM, Yuan Z, et al. TiVCT_x MXene/chalcogenide heterostructure-based high-performance magnesium-ion battery as flexible integrated units. *Small* 2022;18:e2202313. DOI
127. Zhang Y, Cao J, Li J, et al. Self-assembled cobalt-doped NiMn-layered double hydroxide (LDH)/V_2CT_x MXene hybrids for advanced aqueous electrochemical energy storage properties. *Chem Eng J* 2022;430:132992. DOI
128. Pan H, Li B, Mei D, et al. Controlling solid-liquid conversion reactions for a highly reversible aqueous zinc-iodine battery. *ACS Energy Lett* 2017;2:2674-80. DOI
129. Li X, Li N, Huang Z, et al. Enhanced redox kinetics and duration of aqueous I_2/I^- conversion chemistry by MXene confinement. *Adv Mater* 2021;33:e2006897. DOI
130. Wang X, Liu Y, Wei Z, et al. MXene-boosted imine cathodes with extended conjugated structure for aqueous zinc-ion batteries. *Adv Mater* 2022;34:e2206812. DOI
131. Tie Z, Liu L, Deng S, Zhao D, Niu Z. Proton insertion chemistry of a zinc-organic battery. *Angew Chem Int Ed* 2020;59:4920-4. DOI PubMed
132. Na M, Oh Y, Byon HR. Effects of Zn^{2+} and H^+ association with naphthalene diimide electrodes for aqueous Zn-ion batteries. *Chem Mater* 2020;32:6990-7. DOI
133. Nam KW, Park SS, Dos Reis R, et al. Conductive 2D metal-organic framework for high-performance cathodes in aqueous rechargeable zinc batteries. *Nat Commun* 2019;10:4948. DOI PubMed PMC
134. Wang Y, Song J, Wong WY. 3D nanostructured conductive PANI/MXene hydrogels for durable aqueous Zn-ion batteries. *J Mater Chem A* 2024;12:943-9. DOI
135. Wu G, Lv C, Lv W, Li X, Zhang W, Li Z. Anthraquinone derivatives supported by Ti_3C_2(MXene) as cathode materials for aluminum-organic batteries. *J Energy Chem* 2022;74:174-83. DOI
136. Anasori B, Lukatskaya MR, Gogotsi Y. 2D metal carbides and nitrides (MXenes) for energy storage. *Nat Rev Mater* 2017;2:16098. DOI